

Helsinki University of Technology Applied Electronics Laboratory

Series B: Research Reports B7

Teknillisen korkeakoulun sovelletun elektroniikan laboratorio, sarja B: Tutkimusraportteja B7

Espoo 2000

Design and evaluation of Overhauser enhanced MRI visible markers

Raimo Joensuu

TEKNILLINEN KORKEAKOULU
TEKNISKA HÖGSKOLAN
HELSINKI UNIVERSITY OF TECHNOLOGY
UNIVERSITE DE TECHNOLOGIE D'HELSINKI

Helsinki University of Technology Applied Electronics Laboratory
Series B: Research Reports B7

Teknillisen korkeakoulun sovelletun elektroniikan laboratorio, sarja B: Tutkimusraportteja B7
Espoo 2000

Design and evaluation of Overhauser enhanced MRI visible markers

Raimo Joensuu

Dissertation for the degree of Doctor of Technology to be presented with due permission for public examination and debate in Auditorium S4 at Helsinki University of Technology (Espoo, Finland) on the 27th of October, at 12 o'clock noon.

Helsinki University of Technology
Department of Electrical and Communications Engineering
Applied Electronics Laboratory

Teknillinen Korkeakoulu
Sähkö- ja tietoliikennetekniikan osasto
Sovelletun elektroniikan laboratorio

Distribution:

Helsinki University of Technology

Applied Electronics Laboratory

P.O.Box 3000

FIN-02015 HUT, Finland

© Raimo Joensuu

ISBN 951-22-5107-8

ISSN 1456-1174

Otamedia Oy

Espoo 2000

Abstract

This thesis deals with the theoretical principles, design and construction of a small-sized marker which is visible in magnetic resonance images. The nuclear magnetic resonance signal emitted by the marker is enhanced by the use of the Overhauser phenomenon.

Different marker configurations were designed and constructed. A point-like marker was coupled to the feeding cable by loop and loop-gap geometries, and circuit analogies were presented to the loop-gap geometry and to the Overhauser phenomenon. An elongated, cylindrical marker was realized by constructing a transmission-line marker where a microwave shield and tapered coupling were included in the design. The markers' feasibility in interventional use was demonstrated in phantom and *in vitro* experiments, and the loop-gap marker was used in high-resolution MR studies.

Keywords – interventional MRI, device visualization, Overhauser effect

Contents

Abstract

List of publications

The author's contribution

Acknowledgments

Abbreviations

1	Introduction	10
	1.1 General	10
	1.2 Purpose of the study	10
	1.3 Thesis organization	11
2	Review of the literature	11
	2.1 Paramagnetism	11
	2.2 Magnetic resonance	12
	2.3 Relaxation and equation of motion	13
	2.4 Paramagnetic contribution to nuclear relaxation rates	14
	2.4.1 Contrast agents	16
	2.5 Overhauser effect	17
	2.6 Materials' suitability to MR imaging	21
	2.7 Safety in MRI	23
	2.7.1 Magnetic forces and torques	23
	2.7.2 Slowly-varying magnetic fields	23
	2.7.3 Acoustic noise	24
	2.7.4 Radio-frequency radiation	25
	2.8 Instrument visualization techniques	27
	2.8.1 Signal void	27
	2.8.2 Susceptibility-based visualization	27
	2.8.3 Fiducial markers	29
	2.8.4 MR tracking.....	30
	2.8.5 MR profiling	30
	2.8.6 Optical tracking	31
3	Materials and methods	31
	3.1 Overhauser marker	31
	3.2 Marker configurations and coupling schemes	31
	3.3 Microwave shielding	32
4	Results	33
5	Discussion	35
6	References	37

Summary of publications

List of publications

- I R. P. Joensuu, R. E. Sepponen, A. E. Lamminen, C.-G. M. Standertskjöld-Nordenstam, Interventional MR imaging: Demonstration of the feasibility of the Overhauser marker enhancement (OMEN) technique. *Acta Radiologica* 38: 43-46, 1997.
- II R. P. Joensuu, R. E. Sepponen, A. E. Lamminen, S. E. Savolainen, C.-G. M. Standertskjöld-Nordenstam, High-Accuracy MR tracking of interventional devices: The Overhauser Marker Enhancement (OMEN) technique. *Magnetic Resonance in Medicine* 40: 914-921, 1998.
- III R. P. Joensuu, R. E. Sepponen, A. E. Lamminen, C.-G. M. Standertskjöld-Nordenstam, A shielded Overhauser marker for MR tracking of interventional devices. *Magnetic Resonance in Medicine* 43: 139-145, 2000.
- IV R. P. Joensuu, R. E. Sepponen, T. E. Autti, J. I. Tantt, A. E. Lamminen, C.-G. M. Standertskjöld-Nordenstam, A sub-voxel sized Overhauser phantom for high-resolution studies in MRI. Report *B6*, Applied Electronics Laboratory, Helsinki University of Technology, 2000.

The author's contribution

All publications included in this thesis are the results of a group effort. The first author wrote the manuscript for each paper.

In Study I, I designed and built a point-like marker with a simple loop coupling and demonstrated its performance in phantom studies. In Study II, I developed the concept by adding a loop-gap resonator to the circuit, which allowed the matching and tuning of the marker. I presented circuit models for the marker and for the Overhauser phenomenon. In Study III, I designed and built a cylindrical marker which is visible in MR images in all orientations. I designed a microwave shielding to prevent tissue irradiation and a wideband tapered coupling which allowed the use of the same marker in any practical magnetic field strengths. In Study IV, I designed and built a sub-voxel-sized Overhauser phantom and demonstrated its performance in resolution studies.

Acknowledgments

This work was carried out in the Health Care Region of Helsinki and Uusimaa, HUS-röntgen. I am thankful to the Heads of the Department of Radiology, Professor Carl-Gustaf Standertskjöld-Nordenstam and Senior lecturer Jaakko Kinnunen for their invaluable support to my work. I would like to express my deepest gratitude to my supervisor, the Head of the Applied Electronics Laboratory, Professor Raimo Sepponen for the encouragement and support, and I express my sincere thanks to Professor Hannu Eskola and Senior lecturer Gösta Ehnholm for reviewing the manuscript. I thank my co-authors and all the people working in the Department of Radiology.

This work was financially supported by Runar Bäckström Foundation, Instrumentarium Science Foundation, HUCH-Foundation, the Radiological Society of Finland, and Helsinki University Central Hospital.

Helsinki 2000

Raimo Joensuu

Abbreviations

α	angle
β	angle
γ	gyromagnetic ratio
γ_e	electron gyromagnetic ratio
γ_n	nuclear gyromagnetic ratio
$\Delta\chi$	susceptibility difference
ΔB	magnetic flux density difference
Δf	spectral extent
ΔT	temperature change
$\Delta x_i, \Delta y_i, \Delta z_i$	position error inside an object
$\Delta x_e, \Delta y_e, \Delta z_e$	position error outside an object
ε	sign (\pm) of the electron spin quantum number
$\partial/\partial r$	spatial gradient
μ	sign (\pm) of the nuclear spin quantum number
$\vec{\mu}$	magnetic moment
μ_x, μ_y, μ_z	magnetic moment's components along the x , y , and z axes, respectively
μ_i	magnetic permeability inside an object
μ_e	magnetic permeability external to object
ρ	coupling factor, tissue conductivity
σ	electrical conductivity
τ_1	proton longitudinal relaxation time in the presence of the paramagnetic substance
τ_e	constant
τ_p	pulse duration
$1/\tau_1, 1/\tau_2$	observed longitudinal and transverse relaxation rates, respectively
χ	magnetic susceptibility
χ_i	internal magnetic susceptibility
χ_e	external magnetic susceptibility
χ_o	static nuclear susceptibility
χ_{water}	magnetic susceptibility of water
$\Psi_1, \Psi_2, \Psi_3, \Psi_4$	wave functions
ω	angular frequency
ω_1	RF field angular frequency
ω_e	Larmor frequency of the electron spin
$\omega_L, \bar{\omega}_L$	natural precession frequency of a magnetic dipole in the magnetic field
ω_n	Larmor frequency of the nuclear spin
A	constant
B, \vec{B}	magnetic flux density
B_1	amplitude of the RF magnetic flux density
B_{1e}	flux density of the magnetic excitation field
C	specific heat capacity; constant
C_m	nodal capacitance
c	concentration

D	duty cycle
d	nodal gap width, distance
$d\vec{l}$	element of length
dS	element of area
$\frac{d}{dt}$	time derivative
E	energy eigenvalue
\vec{E}	electric field
E_l, E_{l-1}	energy state
E_{inf}	signal enhancement at infinite power level
E_m	dipole's energy
E_{min}	minimum electric field threshold
E_t	threshold electric field strength
e	natural logarithm base
$\vec{e}_x, \vec{e}_y, \vec{e}_z$	unit vectors in Cartesian coordinate system
F_m	magnetic force
f	leakage factor, fiber diameter
FDA	The United States Food and Drug Administration
FOV	field of view
G_a	nodal membrane conductance
G_{readout}	gradient field strength in readout direction
G_{slice}	gradient field strength in slice direction
H_o, \vec{H}_o	static magnetic field strength
H_1	oscillatory magnetic field strength
H_z	z-component of the static magnetic field
\hat{H}	Hamiltonian operator
h	effective thickness
I	nuclear spin quantum number; current
I	nuclear magnetic moment
I_o	thermal equilibrium value of the nuclear magnetic moment
I_z	the component of the nuclear magnetic moment in the static field direction
$\vec{i}', \vec{j}', \vec{k}'$	unit vectors in the laboratory frame of reference
i_{Na}, i_K, i_L, i_p	ionic currents
IEC	International Electrotechnical Commission
J	angular momentum
k	Boltzmann's constant; constant
LD ₅₀	Lethal dose to 50% of the population
M	net magnetization
M_x, M_y, M_z	net magnetization components along the x , y , and z axes, respectively
M_{xy}	transverse magnetization
MR	magnetic resonance
MRI	magnetic resonance imaging
MW	microwave
m	the component of the nuclear magnetic moment in the static field direction, magnetic field per current ratio

m_s, m_l	eigenvalues of electron and nuclear magnetic moments, respectively
N	number of spins
N_+, N_-	number of spins in states $+\frac{1}{2}$ and $-\frac{1}{2}$, respectively
$N_{++}, N_{+-}, N_{-+}, N_{--}$	number of spins in states $ ++\rangle, +-\rangle, -+\rangle, \text{ and } --\rangle$, respectively
NMR	nuclear magnetic resonance
n	difference of number of spins between states $+\frac{1}{2}$ and $-\frac{1}{2}$
n_o	variable
OF	Overhauser factor
P_m	energy level populations
P/V	specific local power loss of the electric field
p, q, r, s	transition probabilities
R	radius
RF	radio-frequency
r	spatial position variable; effective radius
r_1, r_2	longitudinal and transverse relaxivity of the paramagnetic species, respectively
S	electron spin quantum number; saturation factor
\vec{S}	electron magnetic moment
S_o	thermal equilibrium value of the electron spin polarization
S_z	electron magnetic moment's component in the field direction
SAR	specific absorption rate
s	correction factor; tissue specific gravity
T	temperature
T_1	longitudinal relaxation time
T_2	transverse relaxation time
T_{1e}	electron spin longitudinal relaxation time
T_{2e}	electron spin transverse relaxation time
TEM	transverse electric magnetic
TE	time to echo
TR	time of repetition
$1/T_{1para}, 1/T_{2para}$	longitudinal and transverse paramagnetic relaxation rates, respectively
$(1/T_1)_{inner\ sphere}, (1/T_2)_{inner\ sphere}$	longitudinal and transverse nuclear relaxivity due to inner-sphere processes, respectively
$(1/T_1)_{outer\ sphere}, (1/T_2)_{outer\ sphere}$	longitudinal and transverse nuclear relaxivity due to outer-sphere processes, respectively
t	time
t_{SAT}	saturation time
V	volume
V_n	transmembrane voltage
$W\uparrow, W\downarrow$	transition probability per second of a spin from a state $+\frac{1}{2}$ to a state $-\frac{1}{2}$ and from a state $-\frac{1}{2}$ to a state $+\frac{1}{2}$, respectively
$V_{e,n-1}, V_{e,n}, V_{e,n+1}$	external voltage at the $n-1^{th}, n^{th}, \text{ and } n+1^{th}$ node, respectively
$V_{i,n-1}, V_{i,n}, V_{i,n+1}$	internal voltage at the $n-1^{th}, n^{th}, \text{ and } n+1^{th}$ node, respectively
x, y, z	object coordinates
x', y', z'	image coordinates
\hbar	Planck's constant

1 Introduction

1.1 General

The motivation to perform minimally invasive treatments is the ability to circumvent the need for surgery and general anesthesia. Compared to open surgery, in interventional procedures the damage to healthy tissue is minimal, the risk of trauma is decreased, and patient outcome is better. Furthermore, some patients' condition may be such that general anesthesia is not possible (1).

The visibility in minimally invasive procedures is reduced to small incisions only. It is, however, beneficial to have an overall view of the region of interest during the operation to visualize the target tissue together with the surrounding anatomy to ensure the completeness of the operation (2, 3). The combination of medical imaging with the interventional procedure is therefore advantageous.

The first use of human interventional radiology was documented in 1964, when a catheter was used in the transluminal treatment of arteriosclerotic obstruction (4). Today, interventional radiology is common practice. Typical interventional procedures are biopsies and catheterizations, and the imaging methods that are used in interventional radiology are fluoroscopy, ultrasound, angiography, computed tomography (CT) (5), and magnetic resonance (MR) imaging (6).

Magnetic resonance imaging (MRI) has several advantages compared to other imaging modalities. It provides good soft-tissue contrast and easy visualization of vessels at the same time, ionizing radiation is avoided, image contrast can be manipulated, and the imaging plane can be selected freely. MR can also provide functional, perfusion, and flow information. Also, very fast, subsecond imaging sequences are available in commercial imagers. These abilities have been the motivation for the exploration of the possibility of using MR for interventional applications as well. (7-9)

The first procedures in MR guidance were biopsies (9-15), but vascular interventions (16, 17) and MR-guided sinus endoscopy (10, 18, 19) were also tried. The success of the first experiments was limited because they were performed in cylindrical bore magnets with poor patient access during imaging.

Open MR systems together with fast imaging sequences increased the interest in performing interventional procedures in MR guidance (20-31). The direct access to the imaging volume made it possible to perform interventional procedures and acquire imaging information simultaneously. An equally important prerequisite to a successful intervention is the device visualization relative to the area of interest during the procedure. Generating sufficient contrast between the instrument and the surrounding tissue in MRI has turned out to be a challenge.

1.2 Purpose of the study

The aim of this work was to design and construct a marker which:

- is directly visible in MR images
- has its own signal source
- has positional accuracy immune to system nonlinearities
- can be used to locate interventional devices in image-guided procedures in MRI.

1.3 Thesis organization

This thesis consists of four publications and an overview. It is organized into five chapters. The general introduction in Chapter 1 is followed by review of the literature in Chapter 2, which includes the basic principles of nuclear magnetic resonance (NMR), the Overhauser phenomenon, interventional techniques, and safety issues. Chapter 3 describes the different marker configurations; Chapter 4 summarizes the main results, and Chapter 5 concludes the thesis.

2 Review of the literature

2.1 Paramagnetism

Paramagnetic materials possess no magnetic moment in the absence of an external magnetic field but acquire a magnetic moment in the direction of an applied field whose size is a function of the field. A certain class of paramagnetic substances has permanent magnetic moments of atomic or nuclear magnitude (32). The magnetic moment, $\vec{\mu}$, of such substances originates from atoms or molecules with unpaired electrons or nuclei with non-zero angular momentum, \vec{J} . They are related by the equation (33)

$$\vec{\mu} = \gamma \vec{J}, \quad [1]$$

where γ is the gyromagnetic ratio which is a constant of proportionality, and the angular momentum is an integer or a half-integer in units of the Planck's constant, i.e. $\vec{J} = \hbar \vec{l}$. In the absence of a magnetic field the elementary magnetic moments are randomly distributed, but if a paramagnetic sample is placed in a magnetic field, H_o , the magnetic dipoles are distributed in such a way that the substance acquires a net macroscopic magnetization.

The net magnetization of the sample is due to the fact that different orientations of the dipoles, or spins, with respect to the magnetic field correspond to different energies and their populations are unequal. The energy of the dipole in the magnetic field is (33)

$$E_m = -\vec{\mu} \cdot \vec{H}_o = -\mu \hbar m H_o, \quad [2]$$

where $m = I_z$ is the component of the nuclear magnetic moment in the static field direction. Its values are restricted to a series of integer or half-integer values differing by unity between successive values (36).

According to statistical mechanics, the populations P_m of the energy levels are proportional to the Boltzmann factor $e^{-E_m/kT} = e^{\gamma \hbar m H_o/kT}$, where k is Boltzmann's constant and T is the temperature of the lattice. The amount of the magnetization of N spins is the weighted average over all the energy level populations(32)

$$M = N \gamma \hbar \frac{\sum_{m=-I}^I m e^{\frac{\gamma \hbar m H_o}{kT}}}{\sum_{m=-I}^I e^{\frac{\gamma \hbar m H_o}{kT}}}. \quad [3]$$

In nuclear paramagnetism the ratio $\gamma \hbar H_o / kT$ is a small number and it is permissible to linearize the Boltzmann factor (i.e. $e^x \approx 1+x$), and the magnetization of the sample in an external field can be approximated by

$$M = \frac{N \gamma^2 \hbar^2 I(I+1)}{3kT} H_o = \chi_o H_o, \quad [4]$$

where χ_o is the static nuclear susceptibility. (33)

Nuclear magnetic moments are much smaller than those of electrons and the nuclear magnetic contribution to bulk paramagnetism at room temperature is very small. In order to observe nuclear magnetism special methods are required, such as magnetic resonance. (34)

2.2 Magnetic Resonance

A magnetic moment experiences a torque in a magnetic field which is equal to the rate of change of its angular momentum. The equation of motion is described by

$$\frac{d\vec{J}}{dt} = \vec{\mu} \times \vec{H}_o. \quad [5]$$

and its solution in Cartesian coordinates can be found as

$$\begin{aligned} \mu_x &= \mu_o \sin \omega_1 t \sin \omega_L t, \\ \mu_y &= \mu_o \sin \omega_1 t \cos \omega_L t, \\ \mu_z &= \mu_o \cos \omega_1 t, \end{aligned} \quad [6]$$

where $\omega_1 = \gamma B_1$ and the angular momentum has been eliminated by applying Eq. [1] (35). Equation [6] implies that magnetic moment precesses about the magnetic field with angular velocity

$$\vec{\omega}_L = -\gamma \vec{H}_o, \quad [7]$$

where the negative sign indicates that the precession is in the direction of a left-handed screw. This precession produces an oscillatory magnetic moment which can interact with an oscillatory magnetic field $H_1 \cos \omega t$ normal to the static field.

The stationary values of μ along the field are restricted to $\hbar I, \hbar(I-1), \dots$, and allowed transitions are given by the selection rule $\Delta I = \pm 1$ which requires a quantum of energy

$$\hbar \omega = E_I - E_{I-1} = -\gamma \hbar H_o, \quad [8]$$

or

$$\omega = \omega_L. \quad [9]$$

The oscillatory field can interact with the magnetic dipole if its frequency coincides with the natural precession frequency ω_L of the dipole in the magnetic field. This effect is known as magnetic resonance. (33)

2.3 Relaxation and equation of motion

The application of an oscillatory field at the resonance frequency to a macroscopic sample causes the number of its nuclei at different energy states to change. Energy is either absorbed from the alternating field or emitted back into the field depending on whether the transition occurs from a lower energy state to a higher, or vice versa. In both cases the transitions are induced and coherent in phase with the radiation field because the probability of a spontaneous transition at radio frequencies is low. If N_+ and N_- are, respectively, the number of spins in states $+\frac{1}{2}$ and $-\frac{1}{2}$, and denoting the transition probability per second of a spin from a state $+\frac{1}{2}$ to a state $-\frac{1}{2}$ by $w\downarrow$ and the reverse transition by $w\uparrow$, the time variation of the system's magnetization process can be described as (36)

$$\frac{dN_{\pm}}{dt} = N_- w\downarrow - N_+ w\uparrow. \quad [10]$$

Introducing variables $n = N_+ - N_-$ and $N = N_+ + N_-$, N_+ and N_- may be replaced by

$$N_+ = \frac{1}{2}(N + n) \quad [11]$$

$$N_- = \frac{1}{2}(N - n). \quad [12]$$

Substituting this into [10] gives (N is constant)

$$\frac{dn}{dt} = N(w\downarrow - w\uparrow) - n(w\downarrow + w\uparrow) \quad [13]$$

which can be rewritten as

$$\frac{dn}{dt} = \frac{n_o - n}{T_1} \quad [14]$$

where

$$n_o = N \left(\frac{w\downarrow - w\uparrow}{w\downarrow + w\uparrow} \right) \text{ and} \quad [15]$$

$$T_1 = \frac{1}{w\downarrow + w\uparrow}. \quad [16]$$

The solution of Eq. [14] is

$$n = n_o + A e^{-t/T_1}, \quad [17]$$

where A is a constant of integration and T_1 is a characteristic time associated with the nuclear system's approach to thermal equilibrium. It is called the spin-lattice or longitudinal relaxation time, and it is related to the spin system's and the surrounding lattice's microscopic details. (36)

If an external magnetic field acts on a sample of identical interacting spins, the alternating magnetic field of one dipole will affect the resonance transitions of its neighbors. They precess at the same frequency, which produces resonance transitions between spin states and shortens the lifetime of an individual dipole in a given state. The phenomenon is characterized by an exponential decay of the transverse magnetization M_{xy} according to the equation

$$M_{xy}(t) = M_{xy}(0)e^{-\frac{t}{T_2}}, \quad [18]$$

where the constant T_2 is called a spin-spin relaxation time. It describes the finite lifetime of a given state, and it is responsible for the sample's resonance linewidth broadening. Assuming a Lorentzian line shape, the relation between the spin-spin relaxation time and the spectral extent of resonance line Δf is (36)

$$T_2 = 1/(2\pi\Delta f). \quad [19]$$

The equation of motion due to relaxation in external magnetic fields can be described with the aid of the relaxation times by the Bloch equation

$$\frac{d\vec{M}}{dt} = \gamma \vec{M} \times \vec{H} - \frac{M_x \vec{i}' + M_y \vec{j}'}{T_2} - \frac{M_z - M_o}{T_1} \vec{k}', \quad [20]$$

where the static field $H_o = H_z$ and $\vec{i}', \vec{j}', \vec{k}'$ are the unit vectors of the laboratory frame of reference (36).

The relaxation times are sensitive to the physio-chemical environment of the protons and vary considerably between tissues. They are critical in MR imaging because they form the excellent soft-tissue contrast-determining parameters seen with this imaging modality.

2.4 Paramagnetic contribution to nuclear relaxation rates

The addition of a paramagnetic solute into a proton-rich solvent causes an increase in the relaxation rates of solvent nuclei. If no solute-solute interactions occur, the proton relaxation rate increases linearly with the concentration of the paramagnetic species. The efficiency with which the complex enhances the nuclear relaxation rate is called the relaxivity, which is the compound's incremental increase in paramagnetic relaxation rate versus concentration (37)

$$r_i = \frac{1}{T_{i\text{para}}} / c, \quad [21]$$

where c is the concentration and r_i is the longitudinal ($i=1$) or transverse ($i=2$) relaxivity of the paramagnetic species, and $1/T_{i\text{para}}$ is the corresponding paramagnetic relaxation rate. The proton relaxation rate increase is additive to the background relaxation rate in the absence of a paramagnetic species. This may be written as (37)

$$\frac{1}{\tau_i} = \frac{1}{T_i} + \frac{1}{T_{i\text{para}}}, \quad [22]$$

where $1/\tau_i$ is the observed relaxation rate.

Combining Eqs. [21] and [22], the observed relaxation rates can be expressed as

$$\frac{1}{\tau_i} = \frac{1}{T_i} + cr_i. \quad [23]$$

The paramagnetic compound's relaxation enhancement mechanism is related to the substances' one or more unpaired electrons, whose magnetic moment creates a fluctuating local magnetic field providing an additional relaxation pathway for solvent nuclei. The electron's magnetic field is 657 times stronger than that of the proton, and electrons are thus more effective in inducing proton relaxation than nuclei of diamagnetic species. The local field falls off rapidly with distance and therefore translational and chemical mechanisms which bring the nuclei near the solute molecule strongly contribute to the paramagnetic effect (38). Two different relaxation mechanisms have been identified, inner- and outer-sphere relaxation.

The interaction of nuclear relaxivity with respect to the paramagnetic center is classified as inner-sphere relaxation if the fluctuation involves a short-term liganding of the solvent molecules and paramagnetic species. The expressions that characterize this exchange are described by the Solomon-Bloembergen-Morgan equations (39, 40) which indicate that inner-sphere relaxivity increases with the paramagnetic species' concentration, magnetic moment, and the number of solvent molecules which can be bound to the agent (41).

The term outer-sphere relaxation is usually applied if the relaxation mechanism is dominantly due to the relative translational diffusion and there is little binding between the solvent molecules and paramagnetic centers. As with inner-sphere processes, relaxivity increases with the magnetic moment of the paramagnetic species. The relaxation rate is also enhanced with agents where the distance between the nuclear and electron spin is short. Enhancement also occurs if diffusion of the solvent molecules and paramagnetic centers is slow, which indicates long correlation time. (33, 42).

In general, the total relaxivity is given by a combination of inner- and outer-sphere effects

$$\left(\frac{1}{T_i}\right)_{\text{para}} = \left(\frac{1}{T_i}\right)_{\text{inner sphere}} + \left(\frac{1}{T_i}\right)_{\text{outer sphere}} \quad i = 1, 2 \quad [24]$$

where $\left(\frac{1}{T_i}\right)_{\text{inner sphere}}$ and $\left(\frac{1}{T_i}\right)_{\text{outer sphere}}$ are the nuclear relaxation rates due to inner- and outer-sphere processes, respectively (38). Paramagnetic compounds have a similar incremental effect on both nuclear relaxation rates, but the fractional effect on the longitudinal relaxation rate is more prominent since $1/T_2$ is usually much larger than on $1/T_1$. This is beneficial in MR imaging since an increased longitudinal relaxation usually results in increased signal intensity. The magnetization returns to equilibrium in a

shorter time after a radio-frequency (RF) pulse, and the following pulse can be applied more quickly, resulting in a stronger signal for the same collection time. An increased transverse relaxation, on the other hand, reduces signal intensity because of the shortened time available to signal collection. (43)

2.4.1 Contrast agents

Paramagnetic compounds have been widely studied in MRI because of their ability to modify image contrast. Unlike proton density, the relaxation times vary considerably between different tissues and are also sensitive to changes in the physio-chemical environment of the protons. Therefore, the use of pharmaceuticals that shorten protons' relaxation times have the ability to increase the diagnostic utility of MRI. Contrast between isointense but histologically different tissues can be increased, changes in tissue perfusion can be indicated, physiologic function of organs can be studied, pathologies can be characterized, and abnormalities in blood circulation identified. (44-47)

Transition (Fe^{3+} , Mn^{2+} , Cr^{2+} , Cu^{2+} , Ni^{2+}) and lanthanide (Ce^{3+} , Dy^{3+} , Ho^{3+} , Eu^{3+}) metal ions, which have several unpaired electrons, are highly paramagnetic and therefore effective relaxation enhancers (48-52). These metals are, however, relatively toxic and their clearance from tissue is slow. Therefore, they are administered as multidentate chelates to be tolerated, for example diethylenetriaminepentaacetic acid (DTPA) or tetraazacyclododecanetetraacetic acid (DOTA) (52).

Another class of paramagnetic compounds which can be used as contrast agents in MRI is nitroxides. Nitroxides are stable organic free radicals with the general chemical structure depicted in Fig 1. The N-O group is surrounded by four methyl groups, and R can be any group. The paramagnetism of the substance is due to one unpaired electron (depicted as a dot in Fig. 1) which is delocalized between the nitrogen and oxygen atoms. Nitroxides' chemical properties are reviewed in several papers (53-59). Their relaxivities are about ten to fifteen times lower than for Gd-DTPA (60, 61), but the toxicity is low. The LD_{50} values in rats of nitroxides and Gd-DTPA are 15 to 20mmol/kg and 10mmol/kg, respectively (52, 62) and nitroxides' stability is good, which is due to the methyl groups which stabilize the unpaired electron of the nitroxide moiety.

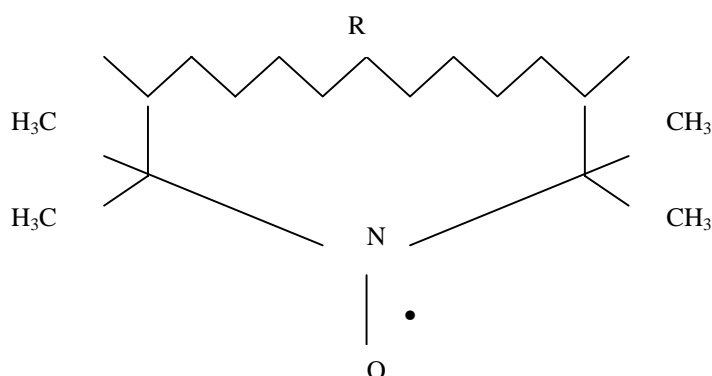


Fig. 1 General chemical structure of nitroxides. The active part of the molecule is the unpaired electron (indicated as a dot). It is responsible for the proton relaxation enhancement, and it is situated in the N-O group which is surrounded by four methyl groups, and a by a group R which can be any group.

Nitroxides are interesting compounds because their electron spin resonance (ESR) lines are narrow and their relaxivities are high, which makes them potential solute candidates for Overhauser enhancement experiments (63-65).

The ESR spectra of the nitroxides have three absorption peaks of equal intensity due to the hyperfine coupling of the magnetic moment of the electron with the nitrogen ^{14}N isotope, an atom with three possible magnetic quantum numbers (-1 , 0 , and $+1$). It reduces the maximum Overhauser enhancement to -110 if only one line is saturated (66). The line widths, which are proportional to the spin-spin relaxation rate, may also change when other paramagnetic species are present, for example molecular oxygen, which is paramagnetic due to its two unpaired electrons (66-69).

2.5 Overhauser effect

The Overhauser effect is a double magnetic resonance technique which requires the presence of two non-identical spins. In the Overhauser experiment, the population distribution of one type of spin is changed and the population distribution of the other spin is observed. This results, in certain conditions, in an increase of the magnitude of the resonance signal of the second spin (70).

Consider the simplest case of a nucleus with spin $I = \frac{1}{2}$ and an electron of spin $S = \frac{1}{2}$, each on different molecules. If the population distribution of nuclei is affected by the population distribution of electrons, and vice versa, the spins are coupled. Such a system is, for instance, a solution of a stable free radical in a proton-containing solvent, where the spins in the solution can diffuse into close proximity of each other. The system's Hamiltonian in an external static magnetic field is (36)

$$\tilde{H} = \gamma_e \hbar H_o S_z + A \vec{I} \cdot \vec{S} - \gamma_n \hbar H_o I_z, \quad [25]$$

where subscripts e and n denote electrons and nuclei, and S_z is the component of the electron magnetic moment in the field direction. Assuming $\gamma_e \hbar H_o \gg A$ (the strong field approximation) the energy eigenvalues are (36)

$$E = \gamma_e \hbar H_o m_s + A m_l m_s - \gamma_n \hbar H_o m_l, \quad [26]$$

where $m_s = \pm \frac{1}{2}$, $m_l = \pm \frac{1}{2}$ are the eigenvalues of S_z and I_z , respectively. The selection rule for induced transitions caused by an applied alternating field is $\Delta m_s = \pm 1$ and $\Delta m_l = 0$, or $\Delta m_s = 0$ and $\Delta m_l = \pm 1$, and the corresponding resonance frequencies are (36)

$$\omega_e = \gamma_e H_o + \frac{A}{\hbar} m_l \quad [27]$$

$$\omega_n = \gamma_n H_o + \frac{A}{\hbar} m_s. \quad [28]$$

There are thus four allowed transitions between the system's energy levels. Distinguishing them by the corresponding wave function (i.e. $\Psi_i = |\epsilon \mu\rangle$ where ϵ and μ

are the signs of the electron and nuclear spin quantum number, respectively) the energy level diagram for the Overhauser effect can be drawn (Fig. 2).

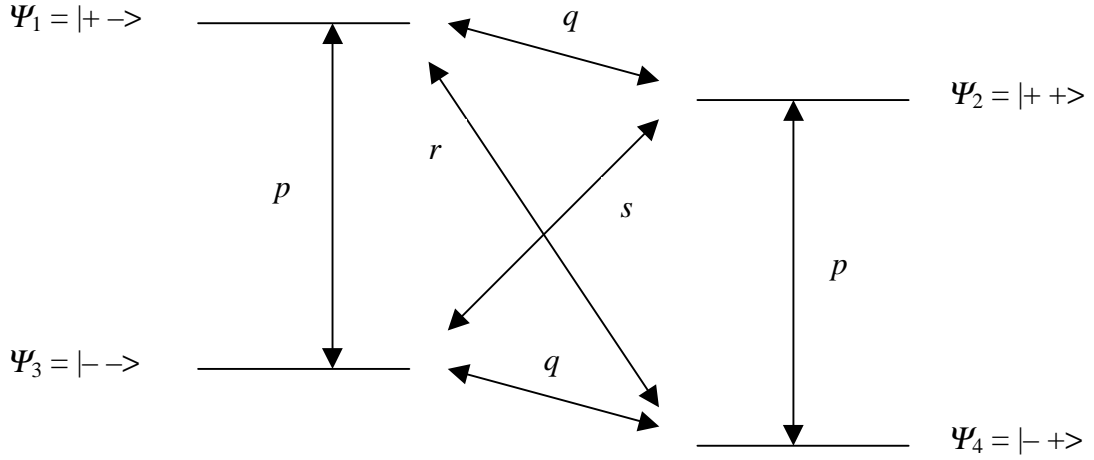


Fig. 2 Spin energy level diagram and possible transitions for a coupled two-spin system. Ψ_i denote the wave functions of the corresponding energy levels where + and – are the signs of the electron and nuclear spin quantum number, and the symbols p , q , r , and s are the transition probabilities (36).

Using the notation from Fig. 2, the rate of population change between the states can be expressed as (36)

$$\frac{dN_{+-}}{dt} = pN_{--} + rN_{-+} + qN_{++} - (p + q + r)N_{+-} + C, \quad [29]$$

where C is a constant. Similar equations for the other energy level populations can be obtained from the thermal equilibrium condition. The components of the electron and nuclear magnetic moments in the field direction are measurable quantities because they are related to the NMR and ESR signals, respectively. The signal strength is proportional to the corresponding population difference by (36)

$$(N_{++} + N_{--}) - (N_{+-} + N_{-+}) = kI_z \quad [30]$$

$$(N_{-+} + N_{--}) - (N_{+-} + N_{++}) = kS_z, \quad [31]$$

where k is a constant of proportionality. Combining Eqs. [29-31], the relaxation of the nuclear spins due to nucleus-electron interactions is described by the equation (36)

$$\frac{dI_z}{dt} = -(2q + r + s)(I_z - I_o) - (r - s)(S_z - S_o), \quad [32]$$

where I_o and S_o are the thermal equilibrium values of the nuclear spin polarization and the electron spin polarization, respectively. A similar equation holds for the relaxation

of electron spins, but the interaction with the nuclear spin is negligible because the electron spins have strong internal relaxation mechanisms.

The term $1/(2q+r+s)$ has a unit of time and it can, as in Eq. [13], be identified as the nuclear spins' characteristic time of the approach to the equilibrium. It is denoted as

$$\tau_1 = \frac{1}{2q+r+s}, \quad [33]$$

where τ_1 is the proton longitudinal relaxation time in the presence of the paramagnetic substance (36).

In the Overhauser experiment the electron spin resonance is saturated. If the ESR saturation is complete ($S_z=0$) and the nuclear magnetization is constant in time ($dI_z/dt=0$), Eq. [32] becomes (36)

$$OF = \frac{I_z - I_o}{I_o} = \frac{r-s}{2q+r+s} \frac{S_o}{I_o}, \quad [34]$$

where OF is the Overhauser factor. The term $(r-s)/(2q+r+s)$ represents the fraction of the polarizing transitions to the total relaxation transitions. It is called the leakage factor and it is denoted by f . Since the polarizing relaxation rate is the inverse of the spin-lattice relaxation time in the radical solution, and the total relaxation rate is the inverse of τ_1 for the solution without free radicals, the leakage factor reduces to (36)

$$f = 1 - \frac{\tau_1}{T_1}. \quad [35]$$

Combining Eqs. [23], [33], and [35] results in the expression (36)

$$f = \frac{cr_1T_1}{1+cr_1T_1}. \quad [36]$$

The second term in Eq. [34], S_o/I_o , is the ratio of electron to nuclear polarization in a steady state, and it gives the theoretical limit to the nuclear signal enhancement. Its numerical value can be found by identifying it to be equal to the ratio of a gyromagnetic factor of an unpaired electron and that of the proton, γ_e/γ_n , which is 658. (36)

Two types of coupling between the electron and nucleus are possible, scalar and dipolar. In scalar coupling the magnetic moment of one spin causes a slight electron polarization of the second spin which, because of electron delocalization, is transmitted to the second nucleus. It can be shown that in the scalar interaction the transitions are induced only parallel to r in Fig. 2, and the coupling factor $\rho=1$. Dipolar coupling is due to molecular motion of one spin at the resonance frequency which induces relaxation transitions to the other spin, and in Fig. 2 the transitions q , r , and s are also allowed. It can be shown that ρ approaches $-\frac{1}{2}$ for a purely dipolar coupling (36).

If the electron spin saturation is incomplete, the nuclear signal enhancement is decreased. The degree of saturation is described by the saturation factor S (36)

$$S = 1 - \frac{S_z}{S_o}. \quad [37]$$

The saturation factor is $S = 1$ when the electron spin populations are equal, and $S = 0$ at the thermal equilibrium. If the magnetization of the electron spins obeys the Bloch equations and the resonance line shape is Lorentzian, the saturation factor can be written as (32)

$$S = \frac{\gamma_e^2 B_{1e}^2 T_{1e} T_{2e}}{1 + \gamma_e^2 B_{1e}^2 T_{1e} T_{2e} + (\omega - \omega_e)^2 T_{2e}^2}, \quad [38]$$

where B_{1e} is the flux density of the magnetic excitation field, T_{1e} and T_{2e} are the electron spin longitudinal and transverse relaxation times, respectively, and ω_e is the Larmor frequency of the electron spin.

The nuclear signal enhancement is decreased if the solute molecule has more than one absorption peak and not all peaks are saturated or due to the molecule's hyperfine structure. These effects are included in the factor E_{inf} . In a steady state the Overhauser factor can therefore be described as (70)

$$OF = E_{\text{inf}} \rho \frac{\gamma_e}{\gamma_n} f S. \quad [39]$$

The nuclear magnetization is built up during the ESR saturation time t_{SAT} with the longitudinal relaxation time τ_1 . Assuming that the equilibrium value of the saturation factor S is reached in a time which is short compared to the nuclear relaxation time, equation [32] can be written as (36)

$$\frac{dI_z}{dt} = -(2q + r + s)(I_z - I_o) + (r - s)SS_o = -\frac{1}{\tau_1}(I_z - I_o - E_{\text{inf}} \rho f S S_o). \quad [40]$$

Combining this with Eq. [39], the differential enhancement equation can be written as

$$\frac{d(OF)}{dt} = -\frac{1}{\tau_1} \left(OF - E_{\text{inf}} \rho f S \frac{\gamma_e}{\gamma_n} \right), \quad [41]$$

which results in the general equation for the Overhauser enhancement (71, 72)

$$OF(t_{\text{SAT}}) = E_{\text{inf}} \rho f S \frac{\gamma_e}{\gamma_n} \left(1 - e^{-\frac{t_{\text{SAT}}}{\tau_1}} \right). \quad [42]$$

It can be seen from Eq. [42] that the build-up of the nuclear magnetization results in a factor $1 - e^{-t_{\text{SAT}}/\tau_1}$ to the static enhancement equation. Therefore, in order to obtain an appreciable increase of the nuclear polarization, it is necessary for the electron spin saturation time to be comparable to or longer than the system's nuclear longitudinal relaxation time in the presence of the electron spin.

2.6 Materials' suitability to MR imaging

The selection of the interventional instrument's materials affects its operation in several ways. The magnetic forces and torques exhibited in certain materials can be a safety hazard (73-78), the device can be a source of image artifacts (34, 79-88), and materials can cause positional misregistrations (88-92).

A material's suitability for interventional use can be predicted from its magnetic susceptibility, χ . It is defined as $M = \chi H$ for those materials whose magnetization depends linearly on the applied field, and it quantifies the material's tendency to interact with and distort an applied magnetic field. (34)

When an object is placed in an initially uniform magnetic field, it becomes magnetized and produces an induced field which distorts the original field. This can lead to image distortion and positional errors because, in the presence of field perturbations, spatial relations present in the object are not necessarily maintained in the image. The distortion can be calculated by solving the Laplace equation for the magnetostatic scalar potential. Analytical solutions can be found for certain geometries (34, 89), and numerical methods have been applied to calculate the fields of irregularly-shaped objects (86, 87, 93).

In the following, equations which describe the distortion for cylindrical and spherical geometries are presented because they most closely resemble the prototype markers which were constructed in this work.

Assume first that the homogeneous magnetic field B_o is oriented in the z direction (Cartesian coordinate system with unit vectors $\vec{e}_x, \vec{e}_y, \vec{e}_z$), the phase encoding in x , the slice selection in y , and the frequency or readout encoding in the z direction. Further assume that a foreign body is placed in the field, with magnetic permeability inside and external to the body μ_i and μ_e , respectively.

If the object is a cylinder with an infinite length and a radius R and the axis in the y direction, the image distortion, defined as the difference between the object's (x, y, z) and the image's coordinates (x', y', z') , is (89)

$$\Delta x_i = 0, \quad [43]$$

$$\Delta y_i = y'_i - y_i = \frac{\Delta\chi}{2} \frac{B_o}{G_{slice}}, \quad [44]$$

$$\Delta z_i = -\frac{\Delta\chi}{2} \frac{B_o}{G_{readout}} \quad [45]$$

inside the cylinder, and

$$\Delta x_e = 0, \quad [46]$$

$$\Delta y_e = \frac{\Delta\chi}{2} \frac{B_o}{G_{slice}} R^2 \frac{z^2 - x^2}{(z^2 + x^2)^2}, \quad [47]$$

$$\Delta z_e = -\frac{\Delta\chi}{2} \frac{B_o}{G_{readout}} R^2 \frac{z^2 - x^2}{(z^2 + x^2)^2} \quad [48]$$

outside the cylinder, where G_{slice} and $G_{readout}$ are the gradient field strengths in slice and readout direction, respectively, and $\Delta\chi = \chi_e - \chi_i$ is the susceptibility difference between the exterior and the interior of the object.

If the cylinder is parallel to the applied magnetic field, the position error inside the cylinder is (34)

$$\Delta x_i = 0, \quad [49]$$

$$\Delta y_i = 0, \quad [50]$$

$$\Delta z_i = \frac{\Delta\chi B_o}{G_{readout}}. \quad [51]$$

There is no image distortion outside the cylinder.

For a sphere, the position error is

$$\Delta x_i = 0, \quad [52]$$

$$\Delta y_i = \frac{2}{3} \Delta\chi \frac{B_o}{G_{slice}}, \quad [53]$$

$$\Delta z_i = -\frac{2}{3} \Delta\chi \frac{B_o}{G_{readout}} \quad [54]$$

for the interior, and

$$\Delta x_e = 0, \quad [55]$$

$$\Delta y_e = \frac{\Delta\chi}{3} \frac{B_o}{G_{slice}} R^3 \frac{2z^2 - x^2 - y^2}{(x^2 + y^2 + z^2)^{3/2}}, \quad [56]$$

$$\Delta z_e = -\frac{\Delta\chi}{3} \frac{B_o}{G_{readout}} R^3 \frac{2z^2 - x^2 - y^2}{(x^2 + y^2 + z^2)^{3/2}} \quad [57]$$

for the exterior (89).

It can be seen from Eqs. [49-57] that the interior of both cylindrical and spherical geometries will be shifted without shape deformation into the direction of the increasing readout gradient. In the exterior, deformation depends on the shape of the object and is a function of the main and gradient field strength and orientation. Strong distortion can cause different voxels to be displayed in the same image pixel, with individual intensities being compounded.

The misregistration is proportional to the susceptibility difference between the object and the surrounding material. The susceptibility of most tissues is close to that of water $\chi_{water} = -9.05 \times 10^{-6}$ ($\pm 10\% \dots 20\%$) (34). Therefore, instruments which are used directly in the imaging region should have a magnetic susceptibility close to tissue in order not to degrade the image quality or reduce the positional accuracy.

2.7 Safety in MRI

MR systems generate three types of electromagnetic fields: the static magnetic field, the time-varying magnetic field gradients, and the radio-frequency field. There are potential hazards involved in all of those field types, and there are a number of regulations and recommendations issued by different agencies whose purpose is to ascertain the safety of magnetic resonance imaging for the patient, the personnel, and the general public (94-96). The motivation to study safety effects in this work are related to the electromagnetic fields' ability to couple to an interventional instrument if its materials or geometry are chosen improperly.

2.7.1 Magnetic forces and torques

Epidemiological studies have shown no significant increase in the prevalence of diseases in humans (97, 98). The only reported physiological effects on subjects exposed to high ($\geq 4\text{T}$) magnetic fields are dizziness and nausea, which have been related to the force on circulating inner ear fluids moving orthogonal to the static magnetic field (99).

A magnetic field can exert an attractive force and/or torque on metallic materials. In this respect, two different regions can be distinguished in a clinical scanner: the homogeneous imaging volume and the inhomogeneous region. The greatest potential risk to patients occurs in the inhomogeneous field region where the field attracts metallic devices in the direction of the field gradient according to (34)

$$F_m = \frac{\chi V}{\mu_0} B \frac{\partial B}{\partial r}, \quad [58]$$

where $\partial B/\partial r$ is the field gradient at the position of the instrument and v is the instrument's volume. As can be seen from Eq. [58], the translational force is proportional to the field strength and its gradient, the volume of the object and its susceptibility.

Magnetic torque tends to align the instrument along the field. There is no simple equation describing this effect because the torque moment depends on the object's volume, shape, susceptibility, and orientation. Unlike the magnetic force, torque does not disappear within the homogeneous field region but ceases to exist only if the object is perfectly aligned with the field. (34)

Ferromagnetic materials can have susceptibility values of tens or hundreds of thousands. Therefore, even small ferromagnetic particles within clinically-used magnetic field strengths can experience large forces and torque moments, and their use in interventional devices has to be excluded (100).

2.7.2 Slowly-varying magnetic fields

A time-varying magnetic field induces electrical currents within a conducting body. The induced electric field, \vec{E} , is related to the time rate of change of flux density according to Faraday's law

$$\oint E \cdot d\vec{l} = -\frac{\partial}{\partial t} \int \vec{B} \cdot d\vec{s}, \quad [59]$$

where $d\vec{l}$ is an element of length along a closed path and $d\vec{s}$ is the element of area normal to the direction of \vec{B} . Magnetically-induced electric fields within a human body have been modeled by assuming that the body is a homogeneous prolate spheroid (101, 102), or a grid of rectangular loops (103).

Slowly-varying magnetic fields in an MR scanner are generated by gradients. The deposited thermal effects are negligible (104), but the induced currents can cause action potentials to nerve fibers (105). The electrical response of the myelinated nerve can be expressed as (106-108)

$$\frac{dV_n}{dt} = \frac{1}{C_m} \left[G_a (V_{i,n-1} - 2V_{i,n} + V_{i,n+1} + V_{e,n-1} - 2V_{e,n} + V_{e,n+1}) - \pi f d (i_{Na} + i_K + i_L + i_p) \right] \quad [60]$$

where C_m is the nodal capacitance, G_a is the nodal membrane conductance, V_n is the transmembrane voltage relative to the resting potential, $V_{e,n}$ is the external voltage at the n^{th} node due to the external stimulus, $V_{i,n}$ is the internal voltage at the n^{th} node, f is the fiber diameter, d is the nodal gap width, and i_{Na} , i_K , i_L , and i_p are ionic currents.

The excitation threshold depends on the external electric field strength as well as its duration according to

$$E_t = E_{\min} \left(1 - e^{-\tau_p/\tau_e} \right)^{-1} \quad [61]$$

where E_t is the threshold electric field strength, E_{\min} is the minimum threshold for long pulses, τ_p is the pulse duration, and τ_e is an experimentally-determined time constant (109).

Among the reported physiological effects of switched-gradient fields are the induction of visual flash sensations (magnetophosphenes) and peripheral nerve and cardiac stimulations. The excitation thresholds are dependent on pulse waveform, frequency, and duration (110-112).

Several regulatory agencies have set limits on the allowable time rate of change of gradient fields. In the International Electrotechnical Commission standard IEC 601-2-33: 1995 three operating modes are defined: the safe level, the mode in which physiological stress may occur, and the level in which significant risk for patients is possible (95). The United States Food and Drug Administration (FDA) sets a general limit on the allowable dB/dt to 20T/s for pulses longer than 120 μ s. FDA regulations allow higher dB/dt values for shorter pulses and higher frequencies if it can be proven that painful stimulation is not induced (96).

2.7.3 Acoustic noise

Gradient coils are energized and de-energized several times per second during the MR imaging process. The alternating gradient fields create resultant forces from the interactions of the static magnetic field and the magnetic field associated with the changing current within the gradient coils. These forces result in motion or vibration of

the gradient coils, which produces a characteristic hammering sound associated with MR scanning. The amplitude of this noise is dependent on the mechanical construction of the magnet, the pulse sequence, and the current waveforms. (113)

Both the IEC and the FDA set limits on the maximum sound pressure levels in areas accessible to patients and give recommendations on the use of ear protection (95, 96).

2.7.4 Radio-frequency radiation

The primary interaction mechanism of radio-frequency fields with the living body is the heating of tissue (114), with consequent biological effects related to the thermally-induced changes in the body (115). Limits of exposure to RF electromagnetic fields have been recommended by several regulatory agencies (95, 96, 116). The purpose of the limits for RF power is to ascertain that RF heating is insufficient to produce hazardous temperature increase in the patient. The safe level set by the FDA is a core temperature increase of less than 1°C, localized temperature less than 38°C in the head, 39°C in the trunk, and 40°C in the extremities (96). Because direct temperature measurement *in vivo* is difficult for individual patients, the generally applied method to limit the temperature increase is to use specific absorption rate (SAR) in units of W/kg.

The local temperature rise caused by the absorbed RF power is (117)

$$\Delta T = \frac{Dt P}{C V}, \quad [62]$$

where D is the duty cycle of the pulse sequence, t is total MRI examination time, C is the specific heat capacity of the object, and P/V is the specific local power loss of the electric field, which can be written as (117)

$$\frac{P}{V} = \left(\frac{1}{8}\right)\sigma\omega^2 B_1^2 s r^2, \quad [63]$$

where σ is the conductivity of the medium, ω is Larmor frequency, B_1 is the amplitude of the RF magnetic flux density, s is a correction factor due to limited RF penetration depth, and r is an effective radius of the object.

The spatial distribution of RF power *in vivo* has been calculated using the impedance method. The human body is modeled by a number of cells whose electromagnetic properties are characterized by the complex impedance, and SAR is calculated for individual cells by applying Faraday's law of induction (118, 119). In the homogeneous model, tissue is approximated by a sphere or a cylinder in which the external RF magnetic field induces eddy current loops. For square excitation pulses the deposited power is

$$P = |\vec{E}|^2 / 2\rho s, \quad [64]$$

where \vec{E} is the induced electric field, ρ is the tissue conductivity, and s is its specific gravity. For non-square RF pulses appropriate correction factors can be found. (104, 120).

A conductive wire, such as an unconnected or malfunctioning surface coil, or the lead of a monitoring device which forms a loop near the patient can cause burn injuries during MR examination (121). The transmitting RF field can couple to the loop,

inducing currents into it. The loop therefore enhances the excitation field strength, and the temperature increase in tissue due to this RF focusing effect can be shown to be

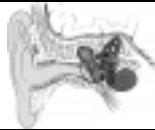
$$\Delta T = \frac{Dt}{C} \frac{8B_1^2}{\sigma\omega^2 h^2 sm^2}, \quad [65]$$

where m is the magnetic field per current ratio and h is the effective thickness of the object (117).

If a straight conductive wire is placed in an RF field, it acts as a dipole antenna and an external electric field can couple TEM relaxation waves along the wire. If the travel time of the TEM wave between the points of reflection matches the frequency of the external RF field, a resonance condition is fulfilled resulting in a build-up of the electrical energy of the TEM wave. The induced current in the wire generates an electric field in the surrounding medium where the field density is highest near the tip of the wire. The maximum tissue temperature is dependent on the field strength, the wire length, and its orientation relative to the RF field. At 1.5T, heating up to 72°C has been measured (122).

Table I summarizes the potential hazards and their mechanisms which are related to static, slowly-varying, and RF fields in MRI.

Table I. Risk sources and their mechanisms in MRI.

Risk source	Mechanism		Result
Static magnetic field			
external ferromagnetic object	projectile		tissue damage
internal ferromagnetic object	motion, torque		tissue damage
Slowly-varying magnetic field			
external	acoustic noise		hearing impairment
internal	neural activation		pain, heart arrhythmia
RF field			
electrically conductive loop 	RF magnetic field focussing		tissue heating
electrically conductive straight wire 	RF electric field focussing		tissue heating

2.8 Instrument visualization techniques

2.8.1 Signal void

A device will displace a certain amount of tissue or blood as it is inserted through the body. This allows one, in principle, to visualize the instrument in an MR image by the dark appearance that arises due to the displacement of tissue spins. However, the device's visibility is determined solely by the image resolution, and thick sections or low in-plane resolution will reduce the contrast between the instrument and the surroundings because the instrument occupies only a small percentage of the volume element. Thick sections are often used when visualizing flexible instruments such as catheters and vascular guidewires because this ensures that the device falls within the imaging plane. Large pixel sizes are often employed in MRI if the image must be rapidly updated, which is needed when the instrument is inserted to compensate the otherwise poor temporal resolution of the imaging method. Thus, instrument visualization based on signal void is, in principle, applicable, but only if the instrument's trajectory is known in advance and thin sections can be used for monitoring the course of intervention (123).

2.8.2 Susceptibility-based visualization

When an object with susceptibility different from that of the surrounding tissue is placed within a homogeneous magnet, local magnetic-field inhomogeneities are introduced. The exact distortion is dependent on the shape of the instrument, and it can be calculated for certain geometries (86, 87, 124). If the object is cylindrical, which is the case in most interventional devices, the local change in the magnetic field outside the object due to the susceptibility difference can be written as (125)

$$\Delta B = B_o \left\{ \vec{e}_x \left[1 + R^2 \left(\frac{\mu_i - \mu_e}{\mu_i + \mu_e} \right) \left(\frac{x^2 - y^2}{(x^2 + y^2)^2} \right) \right] \sin \alpha + \vec{e}_y \left[2R^2 \left(\frac{\mu_i - \mu_e}{\mu_i + \mu_e} \right) \left(\frac{xy}{(x^2 + y^2)^2} \right) \right] \sin \alpha + \vec{e}_z \cos \alpha \right\}, \quad [66]$$

where the angle α represents the orientation of the magnetic field with respect to the object whose axis is assumed to be parallel to the z -axis and R is the radius of the cylinder. The magnetic field inhomogeneity causes geometrical image distortion and intra-voxel dephasing due to the field gradients (89, 126). The dephasing effect is absent in spin-echo sequences because of the refocusing 180° pulse, but the effect is prominent in gradient-echo images.

The susceptibility-induced geometrical distortion in the MR image is given by (89)

$$x' = x + \frac{\Delta B}{G_{readout}} \cos \beta, \quad [67]$$

$$y' = y + \frac{\Delta B}{G_{slice}}, \quad [68]$$

$$z' = z + \frac{\Delta B}{G_{readout}} \sin \beta, \quad [69]$$

where the angle β represents the orientation of the frequency-encoding gradient with respect to the object's axis, and ΔB is given by (34)

$$\Delta B = -B_o R^2 \left(\frac{\mu_i - \mu_e}{\mu_i + \mu_e} \right) \left(\frac{x^2 - y^2}{(x^2 + y^2)^2} \right) \sin^2 \alpha . \quad [70]$$

The susceptibility-induced instrument's visualization is based on the signal loss in the vicinity of the device. The effect is similar to the displacement of spins, but the artifact is larger in magnitude because the signal void extends to the surrounding tissue, and the instrument's visibility in MR images is therefore improved. The magnitude of the artifact also varies in a complicated manner because the effect is dependent on the field strength, the object's material and orientation in the magnetic and gradient fields, and the pulse sequence and sequence parameters used.

Extensive material and geometry studies have been performed to develop an interventional device which creates a suitable-sized artifact (10, 12, 29, 82, 127-133). The artifact must be large enough so that the device can be reliably detected even in thick sections, which are often needed if tortuous vessels are to be covered, but at the same time small enough to allow small lesions to remain visible during the course of intervention.

A limitation of susceptibility-based instrument localization is that it requires a background signal. This may not be a problem in catheters in vessels, but a susceptibility-based instrument location can be ambiguous in low signal regions like the esophagus or lungs. The dependency on the background signal also makes it impossible to locate the instrument outside the body, which would be helpful at the planning stage of an interventional procedure, when an optimal trajectory to the lesion through the parenchyma is chosen. Another limitation is that, similar to the artifact size, the position of the actual instrument may not correspond to the perceived location, but depends on the sequence parameters and the device's orientation in the magnetic field. A displacement factor of 5 times the instrument radius has been reported (125, 134), which limits a reliable targeting of small lesions.

Another method to use the susceptibility effect to obtain contrast between a device and the surroundings is to incorporate a conducting wire onto an instrument and lead electric current through it (135, 136). The current induces a local magnetic field around the wire and, in the case of two antiparallel currents (wires leading to the end of the instrument and back), the magnetic field at a radial position r from the center of wires is

$$B \propto \frac{Id}{\left(\frac{d}{2}\right)^2 - r^2} , \quad [71]$$

where I is the current and d is the distance between the wires (135). The current thus results in a local magnetic field disturbance and a signal cancellation in the vicinity of the wires, which makes it possible to detect the instrument in a MR image. The benefit of this method is that the current strength and the range of the signal loss can be adjusted by controlling the strength of the current. Thus, the artifact can be made large in thick sections and it can be adjusted to be smaller in the vicinity of the target when thin sections are usually applied.

The method has the same limitation as the susceptibility-based methods in general; the technique relies on negative contrast. The instrument is visualized as a domain of

signal loss in the signal-producing spins of the surrounding anatomy, while an appealing alternative would be to render the instrument brighter than the surroundings. In addition to that, it is not evident how much torque the current-carrying wire will experience in a static magnetic field and in the presence of gradients. Nor is it clear whether this will have an effect on the patient safety.

2.8.3 Fiducial markers

It is possible to identify an interventional instrument on the MR images by attaching to it small markers, which contain MR-visible material (fiducials). The NMR signal-emitting markers are not commonly used for instrument localization themselves, because due to their small size they emit only a weak signal and the marker signal is easily lost in the background tissue signal by partial volume effect. There are, however, methods to improve the marker's visibility. One technique is to add a paramagnetic contrast agent into a hydrogen-rich solution. The agent will reduce the solution's relaxation times, and with a proper concentration the transverse relaxation time remains relatively long while the longitudinal relaxation time is short (137). This can be utilized by acquiring MR images with a short repetition time, a short echo time, and a relatively large flip angle. The sequence will saturate the longitudinal magnetization in the surrounding tissue, which will appear dark in MR images, but the marker will recover quickly after each excitation and will remain bright. The marker thus remains visible in thicker and lower resolution slices than without the use of the contrast media, and because the marker contains an internal signal source, it remains visible in air-filled regions as well.

The limitation of the technique is that the selection of usable imaging sequences and sequence parameters are limited, and they are not necessarily optimal for revealing tissue pathology.

Another approach to improve the visibility of fiducials is to wind around it a miniature coil, which is tuned to Larmor frequency. The coil will locally amplify the excitation magnetic field density in the marker, and an external RF field with a small flip angle can therefore result in a substantial rotation of magnetization in the sample (138). The local coil also has high sensitivity for signal detection, which results in a corresponding increase in the observed signal from the fiducial in the images. Winding two coils around the marker in quadrature geometry and tuning them separately can decrease the signal's dependency on the coil's orientation in the main magnetic field. The markers appear brighter than the surrounding tissue if the tissue signal is kept low by a small excitation field. Therefore, the markers are not directly visible together with the background tissue in the same image, but the contrast between the marker and tissue can be controlled, for example, by adjusting the RF flip angle.

A weakness of this technique is related to the tuning of the circuit. The stability of tuning during the course of intervention is critical to the operation of the fiducial. It is not evident how the high permeability of water in tissue will affect the resonator's properties inside tissue. Another limiting factor is that the fiducials will enhance any transmitted and recovered signals, and can therefore disturb the excitation magnetic field in the surrounding tissue and thereby degrade the morphologic accuracy. Also, the increased RF intensity can be a potential safety hazard because it can increase the tissue temperature around the marker to a potentially harmful level.

2.8.4 MR tracking

In MR tracking, the interventional instrument is equipped with a miniature RF coil, which is used to determine the tip location. The built-in coil, usually a short solenoid, has limited spatial extent in all axes, and its position can be found by using a nonselective RF pulse and a gradient-recalled echo along one axis. The localized sensitivity of the coil leads to a single peak in the Fourier-transformed signal, and the position of the peak in the frequency domain corresponds the location of the coil along the gradient axis. The three-dimensional position of the coil is determined by repeating this experiment along all three spatial axes. (28, 131, 139-141) An improvement of the method is to integrate an internal signal source into the coil, which makes the technique insensitive to tissue characteristics, and MR tracking also becomes possible in air-containing structures (142, 143). A Hadamard encoding scheme has been used to collect spatial information in order to compensate positional misregistrations caused by gradient off-resonance effects (144-146).

This technique is very useful for tracking probes that follow curved trajectories, such as catheters or endoscopes. The drawback of this technique is that only the position of a single point on the device is known. The orientation remains thus undetermined, and in order to derive more information about the orientation of the device, multiple coils need to be incorporated. Also, the tracking sequence, which is used for localization, is not suitable for imaging, and positional information needs to be overlaid on a previously-acquired morphologic road map image which is acquired with a separate, conventional RF coil. This makes the method sensitive to motion because if the patient moves during the scan, the position of the catheter may not register correctly and a new road map image must be acquired.

2.8.5 MR profiling

The entire instrument can be visualized if its active part operates as an internal MR antenna (16, 30, 147-149). The antenna acts as a local coil, collecting spatially-encoded signals from the surrounding anatomic structures. The probe is used to transmit RF pulses and receive the RF signal using a fast-imaging sequence with a small field of view to generate a movie of the percutaneous placement procedure of the probe. The movie frames are overlaid onto a previously-acquired road map image where the device can be identified in real time with high signal intensity. The antenna can be made helical which makes the wiring geometry rather insensitive to the orientation to the main magnetic field (150). It may also be a loopless monopole antenna, which is very thin but extends over a length of several centimeters and is therefore particularly suitable for insertion into blood vessels (151, 152).

The limitation of the technique is that the antenna structures do not generate a device outline of limited extent but generally a spatial extent significantly greater than the size of the device itself. Also, the loopless antenna's signal is sensitive to phase-encoding direction, which can result in wrap-around artifacts. Correction algorithms have been developed but they can fail in some orientations (152). Another potential problem is the time separation between the acquisition of the anatomic and the acquisition of the position information, which makes the method vulnerable to patient movements.

2.8.6 Optical tracking

For rigid instruments, such as biopsy needles, to be introduced percutaneously their position inside the body can be projected based on the position and orientation of the part of the instrument, which remains outside the body. The optical-tracking-based frameless stereotaxy systems use tracking of a rigid instrument with a 3D optical digitizer system with two or more video sensors to localize two or more infrared light-emitting diodes (LEDs) mounted on a handheld probe (24). The hand-piece has a fixed relation to the position of the distal end of the instrument, which makes it possible to determine the needle's orientation and the tip's location. This information can be used to overlay the object position and the predicted trajectory onto the MR image, but the positional information of the probe can also be used interactively to select an imaging plane. In practice, multiple orthogonal planes are automatically acquired in real time in relationship to the probe's position. This allows the operator to plan an optimal instrument trajectory to the lesion outside the body preprocedurally, and the progression of the intervention can be followed interactively in near real time (153).

The main drawback of the optical reference system is that it is limited to instruments which follow a linear trajectory to the target. It is therefore not applicable to guiding catheters, endoscopes, or thin needles, which follow curved trajectories, but the interventionist is limited to the use of truly rigid, often traumatic instruments. Another problem is related to the separate acquisition of the anatomic and the position information. This makes the system vulnerable to positional errors, which are related to the MR imager's non-ideal components. These include nonlinearities in shimming, gradient and static magnetic fields, and eddy currents (24). These effects are difficult to compensate and they can limit the smallest lesion that can be targeted by using optical tracking.

3 Materials and methods

3.1 Overhauser marker

The paramagnetic solute that was used in this work was PCA. It has three ESR lines of equal amplitude, resulting from the hyperfine coupling between the electron spin and the spin for the nitrogen atom ($I=1$). In this work only the centerline was saturated whereby the theoretical maximum for NMR signal enhancement is -110 . The contrast agent was prepared by adding 1mM of the solute in 100mM NaOH solution. The solution was degassed with helium before the marker preparation in order to remove paramagnetic oxygen.

3.2 Marker configurations and coupling schemes

In all experiments the marker was attached to the tip of a coaxial cable which conducts saturation energy to the marker. Different coupling geometries were constructed. The simplest configuration is presented in Publication I, where a single-turn loop is wound around the encapsulated marker (Fig. 3a). The coupling is unmatched and a large portion, typically more than 90%, of the incident power is

reflected from the transmission line - marker interface and does not contribute to ESR saturation. High microwave power is therefore needed for NMR signal enhancement.

In Publication II an improvement of the loop geometry is presented (Fig. 3b). A loop-gap resonator is added around the marker and the coupling to the feeding loop is inductive. This configuration enables one to match the marker's impedance to that of the transmission line. The resonator also increases the saturation power density in the marker, which allows the reduction of the incident power level. Circuit analogies are also presented in Publication II for the marker and for the Overhauser enhancement.

In Publication III a transmission line marker geometry is described (Fig. 3c). The marker solution situates between the center conductor and the outer sheath of a coaxial transmission line and the saturation energy is conducted in a form of a TEM wave, which travels through the solution. Impedance matching is accomplished by designing a tapered section at the transmission line - marker interface that matches the marker in a wide bandwidth manner¹.

These marker geometries are referred as simple loop, loop-gap, and transmission line geometry, respectively.

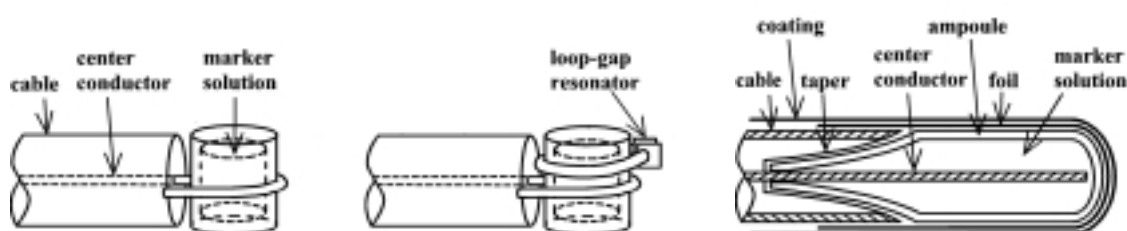


Fig. 3 Schematic drawings of the constructed markers. Left: simple loop, center: loop-gap, and right: transmission line geometry.

3.3 Microwave shielding

A coaxial transmission line conducts the saturation energy hermetically to the marker, but the simple loop and the loop-gap marker structures are unshielded. At the marker the surrounding tissue will therefore be exposed to microwave irradiation which will result in tissue damage unless the saturation power density is kept at a safe level.

In transmission line marker geometry the marker is surrounded by a metallic layer, which creates a galvanic contact with the cable's outer sheath. In this configuration the saturation energy is confined inside the marker and tissue microwave irradiation is negligible. The marker emits an NMR signal, which is detected outside the marker by a conventional receiver coil. The metallic layer must therefore be, at the same time, transparent to low-frequency RF radiation. This is accomplished by making the layer thin. A thin layer will perform as a low-pass filter and by selecting the thickness and conductivity properly the layer can at the same time be made both practically impermeable to high-frequency microwave (MW) and transparent to low-frequency RF radiation.

¹ Patent pending

4 Results

The measured reflection coefficients of different marker geometries are shown in Fig. 4. The impedance mismatch of a simple loop was high throughout the measured frequency range (dashed line), while the addition of a loop-gap resonator tuned and matched the circuit in one frequency (solid line). The resonator circuit's characteristics were also affected by the solution's electron spin resonance, which coupled inductively to the circuit when the marker was placed in a proper magnetic field. The circuit analogy model (Publication II) indicated this effect. Circuit analogy was also presented for the Overhauser phenomenon, which allowed studying of dynamic responses of the NMR signal enhancement (Publication II). The addition of a tapered section in the transmission line marker improved the matching in wide bandwidth (dotted line). Also, because the marker was shielded, its microwave characteristics remained stable independently of changes in the surrounding material's permittivity, for example when the marker was inserted in tissue.

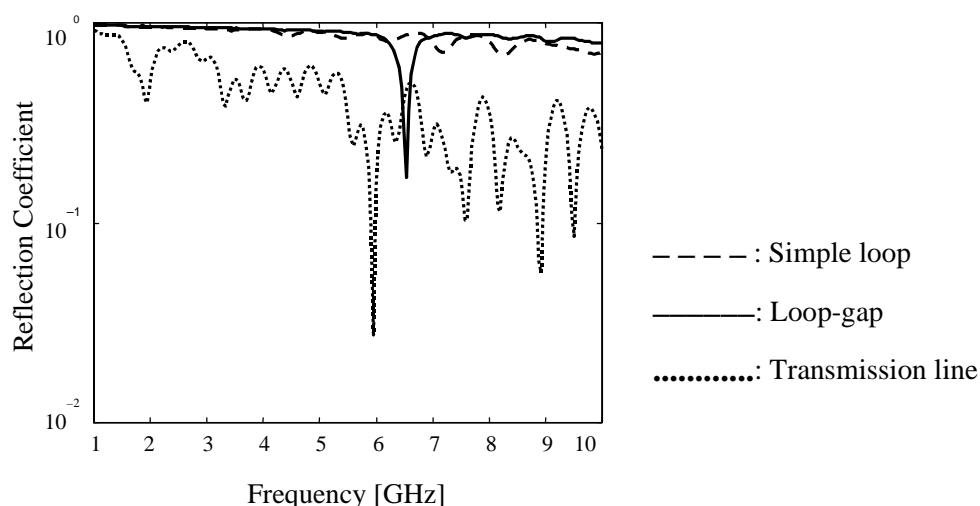


Fig. 4 The measured reflection coefficients of different coupling geometries.

The signal of all the constructed markers were dependent on the markers' orientation in the static field. In simple loop and loop-gap structures the enhanced signal went to zero when the loop's axis was parallel to the main magnetic field. In the transmission line geometry the signal was minimum when the marker's axis was perpendicular and maximum when it was parallel to the static field. NMR signal enhancement was, however, observed in all the marker's orientations in the main field, which could be attributed to the saturating field's distribution pattern in the marker solution (Publication III).

The transmission line marker's temperature was simulated and measured by calorimetric and infrared means as a function of incident power (Publication III). The safe power level, which increases the surrounding tissue's temperature to less than 40°C, was between 0.1 and 0.2 W. The NMR signal enhancement and the marker's visibility were found to be improved by increasing the saturating power beyond that level, but the

marker's temperature raised accordingly, for example at 1W of continuous power the marker's surface temperature exceeded 50°C.

In Fig. 5 two MR images are shown where the marker was inserted in excised animal tissues. On the left is the image of the loop-gap resonator and on the right is the transmission line marker. In the image on the left the marker indicates the instrument's tip, while the cylinder-shaped marker in the image on the right shows also its body, which allows one to make predictions of the marker's future path. The signal enhancement pattern in the transmission line marker is composed of successive high-intensity domains separated by dark areas. This could be explained by the saturating field, which travels through the marker and is reflected back from its tip. The reflected wave acts either constructively or destructively with the incident wave, depending whether they are in phase or in phase opposition. This results in a sinusoidal intensity pattern in the marker at half-wavelength intervals.



Fig. 5 Loop-gap (left) and transmission line markers (right) inserted in excised animal tissues. The instrument's tip is possible to locate by the loop marker construction while the transmission line geometry also allows one to identify the instrument's body. Markers are indicated by arrows. The image on the left was obtained by using a gradient-recalled echo (GRE) sequence with a slice thickness of 4mm, and the image on the right was obtained using an inversion recovery sequence with a slice thickness of 10mm.

In Fig. 6 two MR images acquired with different imaging sequences of a sub-voxel-sized Overhauser marker are shown. The marker is located inside the center pixel which appears brightest in both images. The background signal comes from a large, uniform phantom which was placed behind the sub-voxel marker to provide the offset baseline. The measurement setup also revealed alternating intensity patterns both horizontally and vertically around the sub-voxel marker, which is the system's impulse response (Publication IV).

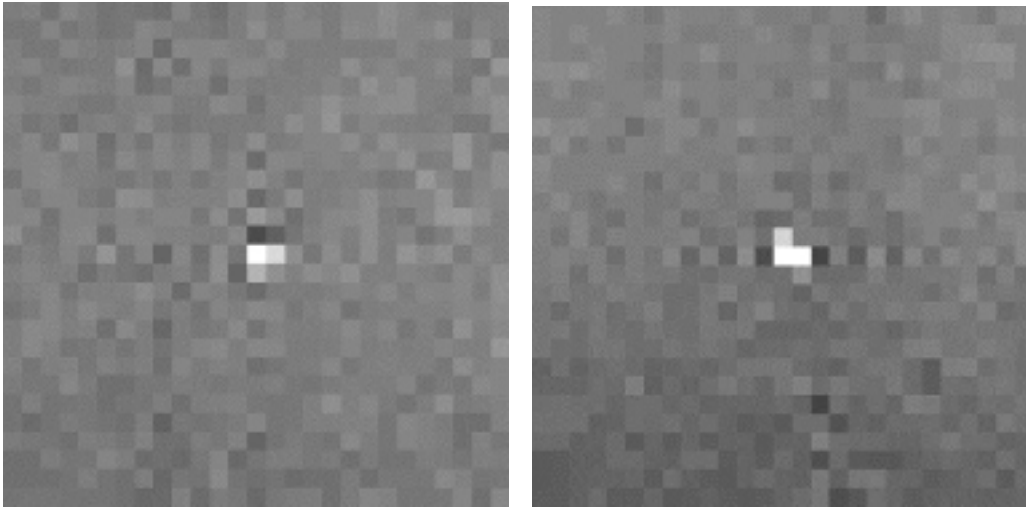


Fig. 6 The imaging system's impulse response. The marker, whose size is smaller than a single voxel, is located in the center. The alternating intensity patterns located horizontally and vertically around the center pixel are the imaging system's impulse response. The image on the left was obtained using a GRE sequence and the image on the right was obtained using a spin echo sequence.

5 Discussion

In this work the development process of an MR-visible Overhauser marker is described.

The simple loop and loop-gap structures are easy to construct, and the marker can be firmly attached to the feeding cable, which makes mechanical construction very robust. The simple loop has the additional benefit of being a non-tuned circuit whereby its microwave performance is only slightly affected by changes in the marker's electromagnetic environment. The impedance mismatch of the simple loop, however, requires that the generator is capable of delivering output power of about 10 - 100 times higher than to a matched circuit in order to achieve the same NMR signal enhancement. The addition of a loop-gap resonator enables one to match the circuit's impedance with that of the transmission line. The resonator circuit also allows the further reduction of the generator's output power requirements. In practice both the electron spin resonance in the marker solution and the surrounding tissue strongly couple to the circuitry, which makes the marker's tuning a challenge. Loop structures in this application also have inherent weaknesses, one of which is the signal's orientation dependency. The signal enhancement goes to zero if the loop's axis is parallel to the main field. The main limitation of the loop structures' use *in vivo* is, however, that saturation energy can irradiate surrounding tissue. It can cause irreversible tissue damage unless microwave power density is kept sufficiently low. No effort was made to quantitatively relate the tissue temperature increase due to microwave irradiation to incident power level, but it was estimated that this effect would seriously limit the attainable NMR signal enhancement.

A microwave-shielded marker is an obvious improvement to the concept. Saturation energy density can be high because it is confined to the marker's interior only. The shield also stabilizes the marker's performance because the microwave field's environment is well defined and stable independently of whether the marker is in air or in tissue. The

shield must be transparent to gradient and RF fields because the marker's positional information is encoded by gradients, and the imager's standard coils are used for the RF excitation and signal detection. This is achieved by choosing a layer thin enough so that it is practically transparent to low-frequency RF but thick enough to keep practically all high-frequency microwave radiation inside the marker. The marker's cylindrical geometry makes it easy to identify in MR images, and it also allows predictions of the marker's future path to be made. This can be a useful property in the planning stage of an interventional procedure and also when targeting small lesions. The marker's oscillating intensity distribution caused by the saturating field's reflection can be utilized by counting the high-intensity nodes from an MR image; if one or some are missing, it is an indication that the marker is partly outside the selected slice. The reflected wave also amplifies the saturation field density by a factor of two at nodal points, which reduces the generator's output requirements by the same factor. The marker's signal is variable but unlike in loop geometries, the transmission line marker emits an enhanced signal in all orientations. The tapered coupling matches the marker in a wide bandwidth and makes it possible to use the same marker in all practical field strengths without adjustments.

The shield protects surrounding tissue from microwave heating. The ampoule insulates the marker thermally from its surroundings and the center conductor transfers heat from the marker into the feeding cable's body. However, saturation energy is absorbed in the lossy marker solution, which will raise the marker's temperature, and heat will flow to the surrounding tissue. The marker's surface temperature currently limits the achievable NMR signal enhancement. The NMR signal can possibly be increased under the given temperature constraints by selecting the marker solution carefully or pulsing the saturation power, but at this stage these methods have not been tried. The conductive wire can cause additional hot spots if the RF transmission field can couple to the wire, but there are proposed methods by which this effect can possibly be reduced (154).

The attractive feature of this marker concept is that it is largely independent of the MR imager's hardware or software. The present concept can be implemented in an existing imager with small or no modifications made to the imager. The marker's position is also immune to system nonlinearities which would affect the device's positional accuracy if indirect localization methods were used. The signal intensity emitted by the marker can be high which allows the marker to be made very small without losing its detectability. However, the signal intensity of the large caliber markers that were constructed in this work may be too large in routine use. Most modern MR imagers scale the signal intensity in images automatically, and an excessively bright marker may cause the background tissue to appear too dark. A high-intensity marker can also cause the analog-to-digital converter to overflow, which can cause artifacts in MR images. Elimination of this effect may require protective modifications in the system's signal acquisition path.

The high signal intensity could be utilized in constructing a sub-voxel-sized phantom. Normally, the signal of such a small phantom would be too low for any practical use, but the Overhauser enhancement allowed it to be imaged even in the presence of a background signal from a 10mm thick 1mM MnCl phantom without excessive partial volume effect. This measurement setup enabled the study of the system's resolution on a single voxel basis.

Two applications of the Overhauser effect have been developed in this work. The sub-voxel phantom concept is readily applicable to resolution studies, and the technical problems related to the interventional marker are believed to be solved, but further work is needed to ascertain the patient safety.

6 References

1. Newman, J. Interventional radiology of the liver and pancreas, *Radiologic Technology*. 70: 513-529, 1999.
2. Black, P. M., Moriarty, T., Alexander, E., 3rd, Stieg, P., Woodard, E. J., Gleason, P. L., Martin, C. H., Kikinis, R., Schwartz, R. B., and Jolesz, F. A. Development and implementation of intraoperative magnetic resonance imaging and its neurosurgical applications, *Neurosurgery*. 41: 831-842; discussion 842-845, 1997.
3. Moriarty, T. M., Kikinis, R., Jolesz, F. A., Black, P. M., and Alexander, E., 3rd Magnetic resonance imaging therapy. Intraoperative MR imaging, *Neurosurgery Clinics of North America*. 7: 323-331, 1996.
4. Dotter, C. T. and Judkins, M. P. Transluminal treatment of arteriosclerotic obstruction. Description of a new technique and a preliminary report of its application., *Circulation*. 30: 654-670, 1964.
5. Allison, D. J. and Pettersson, H. *Interventional Radiology*. Oslo: The NICER Institute, 1994.
6. Jolesz, F. A. Image-guided procedures and the operating room of the future, *Radiology*. 204: 601-612, 1997.
7. Bieze, J. Radiation exposure risks haunt interventionalists, *Diagnostic Imaging*. 8: 68-79, 1993.
8. Wagner, L. K., Eifel, P. J., and Geise, R. A. Potential biological effects following high X-ray dose interventional procedures, *Journal of Vascular and Interventional Radiology*. 5: 71-84, 1994.
9. Lufkin, R. B. Interventional MR imaging, *Radiology*. 197: 16-18, 1995.
10. Lufkin, R., Teresi, L., and Hanafee, W. New needle for MR-guided aspiration cytology of the head and neck, *AJR*. 149: 380-382, 1987.
11. Lufkin, R., Duckwiler, G., Spickler, E., Teresi, L., Chang, M., and Onik, G. MR body stereotaxis: an aid for MR-guided biopsies, *Journal of Computer Assisted Tomography*. 12: 1088-1089, 1988.
12. Lufkin, R., Teresi, L., Chiu, L., and Hanafee, W. A technique for MR-guided needle placement, *AJR*. 151: 193-196, 1988.
13. Lufkin, R. and Layfield, L. Coaxial needle system of MR- and CT-guided aspiration cytology, *Journal of Computer Assisted Tomography*. 13: 1105-1107, 1989.
14. Lufkin, R. B., Robinson, J. D., Castro, D. J., Jabour, B. A., Duckwiler, G., Layfield, L. J., and Hanafee, W. N. Interventional magnetic resonance imaging in the head and neck, *Topics in Magnetic Resonance Imaging*. 2: 76-80, 1990.
15. Trapp, T., Lufkin, R., Abemayor, E., Layfield, L., Hanafee, W., and Ward, P. A new needle and technique for MRI-guided aspiration cytology of the head and neck, *Laryngoscope*. 99: 105-108, 1989.
16. McKinnon, G. C., Debatin, J. F., Leung, D. A., Wildermuth, S., Holtz, D. J., and von Schulthess, G. K. Toward active guidewire visualization in interventional magnetic resonance imaging, *MAGMA*. 4: 13-18, 1996.
17. van Sonnenberg, E., Hajek, P., Gylys-Morin, V., Varney, R. A., Baker, L., Casola, G., Christensen, R., and Mattrey, R. F. A wire-sheath system for

- MR-guided biopsy and drainage: laboratory studies and experience in 10 patients, *AJR*. *151*: 815-817, 1988.
18. Hsu, L., Jolesz, F. A., and Fried, M. P. Interactive MR-guided sinus endoscopy, *Radiology*. *197(P)*: 237, 1995.
 19. Fried, M. P., Hsu, L., Topulos, G. P., and Jolesz, F. A. Image-guided surgery in a new magnetic resonance suite: preclinical considerations, *Laryngoscope*. *106*: 411-417, 1996.
 20. Schenck, J. F., Jolesz, F. A., Roemer, P. B., Cline, H. E., Lorensen, W. E., Kikinis, R., Silverman, S. G., Hardy, C. J., Barber, W. D., Laskaris, E. T., Dorri, B., Newman, R. W., Holley, C. E., Collick, B. D., Dietz, D. P., Mack, D. C., Ainslie, M. D., Jaskolski, P. L., Figueira, M. R., vomLehn, J. C., Souza, S. P., Dumoulin, C. L., Darrow, R. D., StPeters, R. L., Rohling, K. W., Watkins, R. D., Eisner, D., R., Blumenfeld, S. M., and Vosburgh, K. G. Superconducting open-configuration MR imaging system for image-guided therapy, *Radiology*. *195*: 805-814, 1995.
 21. Hagspiel, K. D., Kandarpa, K., and Silverman, S. G. Interactive MR-guided percutaneous nephrostomy, *Journal of Magnetic Resonance Imaging*. *8*: 1319-1322, 1998.
 22. Kettenbach, J., Silverman, S. G., Hata, N., Kuroda, K., Saiviroonporn, P., Zientara, G. P., Morrison, P. R., Hushek, S. G., Black, P. M., Kikinis, R., and Jolesz, F. A. Monitoring and visualization techniques for MR-guided laser ablations in an open MR system, *Journal of Magnetic Resonance Imaging*. *8*: 933-943, 1998.
 23. Wong, T. Z., Silverman, S. G., Fielding, J. R., Tempany, C. M., Hynynen, K., and Jolesz, F. A. Open-configuration MR imaging, intervention, and surgery of the urinary tract, *Urologic Clinics of North America*. *25*: 113-122, 1998.
 24. Silverman, S. G., Collick, B. D., Figueira, M. R., Khorasani, R., Adams, D. F., Newman, R. W., Topulos, G. P., and Jolesz, F. A. Interactive MR-guided biopsy in an open-configuration MR imaging system, *Radiology*. *197*: 175-181, 1995.
 25. Silverman, S. G., Jolesz, F. A., Newman, R. W., Morrison, P. R., Kanan, A. R., Kikinis, R., Schwartz, R. B., Hsu, L., Koran, S. J., and Topulos, G. P. Design and implementation of an interventional MR imaging suite, *AJR*. *168*: 1465-1471, 1997.
 26. Orel, S. G., Schnall, M. D., Newman, R. W., Powell, C. M., Torosian, M. H., and Rosato, E. F. MR imaging-guided localization and biopsy of breast lesions: initial experience, *Radiology*. *193*: 97-102, 1994.
 27. Lu, D. S., Sinha, S., Lucas, J., Farahani, K., Lufkin, R., and Lewin, K. MR-guided percutaneous ethanol ablation of liver tissue in a .2-T open MR system: preliminary study in porcine model, *Journal of Magnetic Resonance Imaging*. *7*: 303-308, 1997.
 28. Dumoulin, C. L., Souza, S. P., and Darrow, R. D. Real-time position monitoring of invasive devices using magnetic resonance, *Magnetic Resonance in Medicine*. *29*: 411-415, 1993.
 29. Bakker, C. J., Hoogeveen, R. M., Weber, J., Vaals, J. J. v., Viergever, M. A., and Mali, W. P. Visualization of dedicated catheters using fast scanning techniques with potential for MR-guided vascular interventions, *Magnetic Resonance in Medicine*. *36*: 816-820, 1996.

30. Ladd, M. E., Erhart, P., Debatin, J. F., Hofmann, E., Boesiger, P., von Schulthess, G. K., and McKinnon, G. C. Guidewire antennas for MR fluoroscopy, *Magnetic Resonance in Medicine*. 37: 891-897, 1997.
31. Leung, D. A., Debatin, J. F., Wildermuth, S., Heske, N., Dumoulin, C. L., Darrow, R. D., Hauser, M., Davis, C. P., and Schulthess, G. K. v. Real-time biplanar needle tracking of interventional MR imaging procedures, *Radiology*. 197: 485-488, 1995.
32. Abragam, A. and Bleaney, B. *Electron Paramagnetic Resonance of Transition Ions*. Oxford: Clarendon Press, 1970.
33. Abragam, A. *Principles of nuclear magnetism*. Oxford: Oxford University Press, 1961.
34. Schenck, J. F. The role of magnetic susceptibility in magnetic resonance imaging: MRI magnetic compatibility of the first and second kinds, *Medical Physics*. 23: 815-850, 1996.
35. Callaghan, P. T. *Principles of Nuclear Magnetic Resonance Microscopy*. New York: Oxford University Press Inc., 1995.
36. Slichter, C. P. *Principles of Magnetic Resonance*, 3rd edition. New York: Springer-Verlag, 1990.
37. Bennett, H. F. Effect of nitroxides and molecular oxygen on proton relaxation rates in aqueous systems and lipids. Department of Nuclear engineering. Urbana: University of Illinois, USA, 1988.
38. Lauffer, R. B. Paramagnetic metal complexes as water proton relaxation agents for NMR imaging: Theory and design, *Chemical Reviews*. 87: 901-927, 1987.
39. Solomon, I. Relaxation processes in a system of two spins, *Physical Review*. 99: 559-565, 1955.
40. Bloembergen, N. and Morgan, L. O. Proton relaxation times in paramagnetic solutions. Effects of electron spin relaxation, *The Journal of Chemical Physics*. 34: 842-850, 1961.
41. Koenig, S. H. and Brown, R. D. d. Relaxation of solvent protons by paramagnetic ions and its dependence on magnetic field and chemical environment: implications for NMR imaging, *Magnetic Resonance in Medicine*. 1: 478-495, 1984.
42. Bloembergen, N., Purcell, E. M., and Pound, R. V. Relaxation effects in nuclear magnetic resonance absorption, *Physical Review*. 73: 679-712, 1948.
43. Wehrli, F. W., MacFall, J. R., Shutts, D., Breger, R., and Herfkens, R. J. Mechanism of contrast in NMR imaging, *Journal of Computed Assisted Tomography*. 8: 369-380, 1984.
44. Brasch, R. C. Methods of contrast enhancement for NMR imaging and potential applications, *Radiology*. 147: 781-788, 1983.
45. Cameron, I. L., Ord, V. A., and Fullerton, G. D. Characterization of proton NMR relaxation times in normal and pathological tissues by correlation with other tissue parameters, *Magnetic Resonance Imaging*. 2: 97-106, 1984.
46. Wehrli, F. W., MacFall, J. R., Glover, G. H., Grigsby, N., Haughton, V., and Johanson, J. The dependence of nuclear magnetic resonance (NMR) image contrast on intrinsic and pulse sequence parameters, *Magnetic Resonance Imaging*. 2: 3-16, 1984.

47. Engelstad, B. L. and Brasch, R. C. Pharmaceutical development for magnetic resonance imaging. *In: T. L. James and A. R. Margulis (eds.), Biomedical Magnetic Resonance*, 139-156. San Francisco: Radiology Research and Education Foundation, 1985.
48. Runge, V. M., Clanton, J. A., Foster, M. A., Smith, F. W., Lukehart, C. M., Jones, M. M., Partain, C. L., and James, A. E., Jr. Paramagnetic NMR contrast agents. Development and evaluation, *Investigative Radiology*. *19*: 408-415, 1984.
49. Runge, V. M., Clanton, J. A., Herzer, W. A., Gibbs, S. J., Price, A. C., Partain, C. L., and James, A. E., Jr. Intravascular contrast agents suitable for magnetic resonance imaging, *Radiology*. *153*: 171-176, 1984.
50. Runge, V. M., Clanton, J. A., Lukehart, C. M., Partain, C. L., and James, A. E., Jr. Paramagnetic agents for contrast-enhanced NMR imaging: a review, *AJR*. *141*: 1209-1215, 1983.
51. Runge, V. M., Stewart, R. G., Clanton, J. A., Jones, M. M., Lukehart, C. M., Partain, C. L., and James, A. E., Jr. Work in progress: potential oral and intravenous paramagnetic NMR contrast agents, *Radiology*. *147*: 789-791, 1983.
52. Weinmann, H. J., Brasch, R. C., Press, W. R., and Wesbey, G. E. Characteristics of gadolinium-DTPA complex: a potential NMR contrast agent, *AJR*. *142*: 619-624, 1984.
53. McConnell, H. M. and McFarland, G. B. Physics and chemistry of spin labels, *Quarterly Review of Biophysics*. *3*: 91-136, 1970.
54. Rozantsev, E. G. and Shoile, V. D. Synthesis and reactions of stable nitroxyl radicals I. Reactions, *Synthesis*. 401-414, 1971.
55. Rozantsev, E. G. and Shoile, V. D. Synthesis and reactions of stable nitroxyl radicals I. Synthesis, *Synthesis*. 190-202, 1971.
56. Keana, J. F. W. Newer aspects of the synthesis and chemistry of nitroxide spin labels, *Chemical Reviews*. *78*: 37-64, 1978.
57. Keana, J. F. W. New aspects of nitroxide chemistry. *In: L. J. Berliner (ed.) Spin Labeling. Theory and Applications*, *2*: 115-172. New York: Academic Press, 1979.
58. Keana, J. F. and Van Nice, F. L. Influence of structure on the reduction of nitroxide MRI contrast-enhancing agents by ascorbate, *Physiological Chemistry & Physics & Medical NMR*. *16*: 477-480, 1984.
59. Gaffney, B. J. The chemistry of spin labels. *In: L. J. Berliner (ed.) Spin Labeling. Theory and Applications*, *1*: 183-238. New York: Academic Press, 1976.
60. Ehman, R. L., Wesbey, G. E., Moon, K. L., Williams, R. D., McNamara, M. T., Couet, W. R., Tozer, T. N., and Brasch, R. C. Enhanced MRI of tumors utilizing a new nitroxyl spin label contrast agent, *Magnetic Resonance Imaging*. *3*: 89-97, 1985.
61. Lovin, J. D., Wesbey, G. E., Engelstad, B. L., Sosnovsky, G., Moseley, M., Tuck, D. L., and Brasch, R. C. Magnetic field dependence of spin-lattice relaxation enhancement using piperidiny nitroxyl spin-labels, *Magnetic Resonance Imaging*. *3*: 73-81, 1985.
62. Afzal, V., Brasch, R. C., Nitecki, D. E., and Wolff, S. Nitroxyl spin label contrast enhancers for magnetic resonance imaging. Studies of acute toxicity and mutagenesis, *Investigative Radiology*. *19*: 549-552, 1984.

63. Ardenkjaer-Larsen, J. H., Laursen, I., Leunbach, I., Ehnholm, G., Wistrand, L. G., Petersson, J. S., and Golman, K. EPR and DNP properties of certain novel single electron contrast agents intended for oximetric imaging, *Journal of Magnetic Resonance*. *133*: 1-12, 1998.
64. Low, W. Paramagnetic resonance in solids. *In*: F. Seitz and D. Turnbull (eds.), *Solid State Physics, Advances in Research and Applications*, supp. 2. New York: Academic Press, 1960.
65. Grucker, D., Guiberteau, T., Eclancher, B., Chambron, J., Chiarelli, R., Rassat, A., Subra, G., and Gallez, B. Dynamic nuclear polarization with nitroxides dissolved in biological fluids, *Journal of Magnetic Resonance B*. *106*: 101-109, 1995.
66. Morrish, A. H. *The Physical Principles of Magnetism*. New York: McGraw-Hill, 1965.
67. Popp, C. A. and Hyde, J. S. Effect of oxygen on EPR spectra of nitroxide spin-label probes of model membranes, *Journal of Magnetic Resonance*. *43*: 249-258, 1981.
68. Freed, J. H. Theory of slow tumbling ESR spectra for nitroxides. *In*: L. J. Berliner (ed.) *Spin Labeling. Theory and Applications*, *1*: 53-132. New York: Academic Press, 1976.
69. Jost, P. and Griffith, O. H. Instrumental aspects of spin labeling. *In*: L. J. Berliner (ed.) *Spin Labeling. Theory and Applications*, 251-272. New York: Academic Press, 1976.
70. Overhauser, A. W. Polarization of nuclei in metals. *Physical Review* *92*: 411-415. 1953.
71. Konijnenburg, H. and Vujcic, T. Overhauser imaging: requirements, design, specification and verification. Ph.D diss. Technische Universiteit Delft, Delft, Netherland. 1998.
72. Golman, K., Leunbach, I., Ardenkjaer-Larsen, J. H., Ehnholm, G. J., Wistrand, L. G., Petersson, J. S., Jarvi, A., and Vahasalo, S. Overhauser-enhanced MR imaging (OMRI), *Acta Radiologica*. *39*: 10-17, 1998.
73. New, P. F., Rosen, B. R., Brady, T. J., Buonanno, F. S., Kistler, J. P., Burt, C. T., Hinshaw, W. S., Newhouse, J. H., Pohost, G. M., and Taveras, J. M. Potential hazards and artifacts of ferromagnetic and nonferromagnetic surgical and dental materials and devices in nuclear magnetic resonance imaging, *Radiology*. *147*: 139-148, 1983.
74. Becker, R. L., Norfray, J. F., Teitelbaum, G. P., Bradley, W. G., Jr., Jacobs, J. B., Wacaser, L., and Rieman, R. L. MR imaging in patients with intracranial aneurysm clips, *Ajnr: American Journal of Neuroradiology*. *9*: 885-889, 1988.
75. Teitelbaum, G. P., Bradley, W. G., Jr., and Klein, B. D. MR imaging artifacts, ferromagnetism, and magnetic torque of intravascular filters, stents, and coils, *Radiology*. *166*: 657-664, 1988.
76. Shellock, F. G. Biological effects and safety aspects of magnetic resonance imaging, *Magnetic Resonance Quarterly*. *5*: 243-261, 1989.
77. Kanal, E., Shellock, F. G., and Talagala, L. Safety considerations in MR imaging, *Radiology*. *176*: 593-606, 1990.
78. Shellock, F. G. MR imaging of metallic implants and materials: a compilation of the literature, *AJR*. *151*: 811-814, 1988.

79. Cox, I. J., Bydder, G. M., and Gadian, D. G. The effect of magnetic susceptibility variations in NMR imaging and NMR spectroscopy in vivo, *Journal of Magnetic Resonance*. *70*: 163-168, 1986.
80. Park, H. W., Ro, Y. M., and Cho, Z. H. Measurement of the magnetic susceptibility effect in high-field NMR imaging, *Physics in Medicine & Biology*. *33*: 339-349, 1988.
81. Czervionke, L. F., Daniels, D. L., Wehrli, F. W., Mark, L. P., Hendrix, L. E., Strandt, J. A., Williams, A. L., and Haughton, V. M. Magnetic susceptibility artifacts in gradient-recalled echo MR imaging, *AJNR: American Journal of Neuroradiology*. *9*: 1149-1155, 1988.
82. Farahani, K., Sinha, U., Sinha, S., Chiu, L. C. L., and Lufkin, R. B. Effect of field strength on susceptibility artifacts in magnetic resonance imaging, *Computerized Medical Imaging and Graphics*. *14*: 409-413, 1990.
83. Posse, S. and Aue, W. P. Susceptibility artifacts in spin-echo and gradient-echo imaging, *Journal of Magnetic Resonance*. *88*: 473-492, 1990.
84. Yamada, N., Imakita, S., Sakuma, T., Nishimura, Y., Yamada, Y., Naito, H., Nishimura, T., and Takamiya, M. Evaluation of the susceptibility effect on the phase images of a simple gradient echo, *Radiology*. *175*: 561-565, 1990.
85. Pope, J. M., Walker, R. R., and Kron, T. Artifacts in chemical shift selective imaging, *Magnetic Resonance Imaging*. *10*: 695-698, 1992.
86. Bhagwandien, R., van Ee, R., Beersma, R., Bakker, C. J., Moerland, M. A., and Lagendijk, J. J. Numerical analysis of the magnetic field for arbitrary magnetic susceptibility distributions in 2D, *Magnetic Resonance Imaging*. *10*: 299-313, 1992.
87. Bakker, C. J., Moerland, M. A., Bhagwandien, R., and Beersma, R. Analysis of machine-dependent and object-induced geometric distortion in 2DFT MR imaging, *Magnetic Resonance Imaging*. *10*: 597-608, 1992.
88. Sumanaweera, T. S., Adler, J. R., Jr., Napel, S., and Glover, G. H. Characterization of spatial distortion in magnetic resonance imaging and its implications for stereotactic surgery, *Neurosurgery*. *35*: 696-703; discussion 703-704, 1994.
89. Ludeke, K. M., Röschmann, P., and Tischler, R. Susceptibility artefacts in NMR imaging, *Magnetic Resonance Imaging*. *3*: 329-343, 1985.
90. Kondziolka, D., Dempsey, P. K., Lunsford, L. D., Kestle, J. R., Dolan, E. J., Kanal, E., and Tasker, R. R. A comparison between magnetic resonance imaging and computed tomography for stereotactic coordinate determination, *Neurosurgery*. *30*: 402-406; discussion 406-407, 1992.
91. Sumanaweera, T. S., Adler, J. R., Glover, G. H., Hemler, P. F., van den Elsen, P. A., Martin, D., and Napel, S. Method for correcting magnetic resonance image distortion for frame-based stereotactic surgery, with preliminary results, *Journal of Image Guided Surgery*. *1*: 151-157, 1995.
92. Sumanaweera, T. S., Glover, G. H., Hemler, P. F., van den Elsen, P. A., Martin, D., Adler, J. R., and Napel, S. MR geometric distortion correction for improved frame-based stereotaxic target localization accuracy, *Magnetic Resonance in Medicine*. *34*: 106-113, 1995.
93. Bhagwandien, R., Moerland, M. A., Bakker, C. J. G., Beermsa, R., and Lagendijk, J. J. W. Numerical analysis of the magnetic field for arbitrary

- magnetic susceptibility distributions in 3D, *Magnetic Resonance Imaging*. 12: 101-107, 1994.
94. Biological Evaluation of Medical Devices. Part 1: Evaluation and Testing. Genève: International Electrotechnical Commission (IEC), 1995.
95. Medical electrical equipment. Part 2: Particular requirements for the safety of magnetic resonance equipment for medical diagnosis. Genève: International Electrotechnical Commission (IEC), 1995.
96. Guidance for the submission of premarket notifications for magnetic resonance diagnostic devices. U.S. Department of Health and Humans Services, Food and Drug Administration (FDA), Center for Devices and Radiological Health, 1998.
97. Milham, S., Jr. Mortality in aluminum reduction plant workers, *Journal of Occupational Medicine*. 21: 475-480, 1979.
98. Rockette, H. E. and Arena, V. C. Mortality studies of aluminum reduction plant workers: potroom and carbon department, *Journal of Occupational Medicine*. 25: 549-557, 1983.
99. Budinger, T. F. Emerging nuclear magnetic resonance technologies. Health and safety. *In*: R. L. Magin, R. P. Liburdy, and B. Persson (eds.), *Biological Effects and Safety Aspects of Nuclear Magnetic Resonance Imaging and Spectroscopy*, 649: 188-203. New York: The New York Academy of Sciences, 1992.
100. Planert, J., Modler, H., and Vosshenrich, R. Measurements of magnetism-related forces and torque moments affecting medical instruments, implants, and foreign objects during magnetic resonance imaging at all degrees of freedom, *Medical Physics*. 23: 851-856, 1996.
101. Durney, C. H., Johnson, C. C., and Massoudi, H. Long wavelength analysis of plane wave irradiation of a prolate spheroid model of a man, *IEEE Transactions on Microwave Theory and Techniques*. 23: 246-253, 1975.
102. Spiegel, R. J. Magnetic coupling to a prolate spheroid model of a man, *IEEE Transactions on Power Apparatus and Systems*. 96: 208-212, 1977.
103. Gandhi, O. P., DeFord, J. F., and Danai, H. Impedance method for calculation of power deposition patterns in magnetically induced hyperthermia, *IEEE Transactions on Biomedical Engineering*. 31: 644-651, 1984.
104. Bottomley, P. A. and Edelstein, W. A. Power deposition in whole-body NMR imaging, *Medical Physics*. 8: 510-512, 1981.
105. Reilly, J. P. Principles of nerve and heart excitation by time-varying magnetic fields. *In*: R. L. Magin, R. P. Liburdy, and B. Persson (eds.), *Biological effects and safety aspects of nuclear magnetic resonance imaging and spectroscopy*, 649: 96-117. New York: The New York Academy of Sciences, 1992.
106. Frankenhauser, B. and Huxley, A. F. The action potential in the myelinated nerve fiber of *Xenopus laevis* as computed on the basis of voltage clamp data, *Journal of Physiology*. 171: 302-315, 1964.
107. McNeal, D. R. Analysis of a model for excitation of myelinated nerve, *IEEE Transactions on Biomedical Engineering*. 23: 329-337, 1976.

108. Reilly, J. P. Peripheral nerve stimulation by induced electric currents: exposure to time-varying magnetic fields, *Medical & Biological Engineering & Computing*. 27: 101-110, 1989.
109. Reilly, J. P. and Larkin, W. D. Electrocutaneous stimulation with high voltage capacitive discharges, *IEEE Transactions on Biomedical Engineering*. 30: 631-641, 1983.
110. Budinger, T. F. Thresholds for physiological effects due to RF and magnetic fields used in NMR imaging, *IEEE Transactions on Nuclear Science*. 26: 2821-2825, 1979.
111. Budinger, T. F., Fischer, H., Hentschel, D., Reinfelder, H. E., and Schmitt, F. Physiological effects of fast oscillating magnetic field gradients, *Journal of Computer Assisted Tomography*. 15: 909-914, 1991.
112. Budinger, T. F. Nuclear magnetic resonance (NMR) in vivo studies: known thresholds for health effects, *Journal of Computer Assisted Tomography*. 5: 800-811, 1981.
113. Kanal, E. An overview of electromagnetic safety considerations associated with magnetic resonance imaging. *In: R. L. Magin, R. P. Liburdy, and B. Persson (eds.), Biological Effects and Safety Aspects of Nuclear Magnetic Resonance Imaging and Spectroscopy*, 649: 204-224. New York: The New York Academy of Sciences, 1992.
114. Grandolfo, M., Polichetti, A., Vecchia, P., and Gandhi, O. P. Spatial distribution of RF power in critical organs during magnetic resonance imaging. *In: R. L. Magin, R. P. Liburdy, and B. Persson (eds.), Biological effects and safety aspects of nuclear magnetic resonance imaging and spectroscopy*, 649: 176-187. New York: The New York Academy of Sciences, 1992.
115. Cleary, S. F., Liu, L.-M., and Cao, G. Effects of RF power absorption in mammalian cells. *In: R. L. Magin, R. P. Liburdy, and B. Persson (eds.), Biological effects and safety aspects of nuclear magnetic resonance imaging and spectroscopy*, 649: 166-175. New York: The New York Academy of Sciences, 1992.
116. Guidelines on limits of exposure to radiofrequency electromagnetic fields in the frequency range from 100kHz to 300GHz. *Health Physics*, 54: 115-123: International Non-Ionizing Radiation Committee of the International Radiation Protection Association INIRC/IRPA, 1988.
117. Boesiger, P., Buchli, R., Saner, M., and Meier, D. Increased radio-frequency power absorption in human tissue due to coupling between body coil and surface coil. *In: R. L. Magin, R. P. Liburdy, and B. Persson (eds.), Biological effects and safety aspects of nuclear magnetic resonance imaging and spectroscopy*, 649: 160-165. New York: The New York Academy of Sciences, 1992.
118. deFord, J. F. and Gandhi, O. P. An impedance method to calculate currents induced in biological bodies exposed to quasi-static electromagnetic fields, *IEEE Transactions on Electromagnetic Compatibility*. 27: 168-173, 1985.
119. Orcutt, N. and Gandhi, O. P. A 3-D impedance method to calculate power deposition in biological bodies subject to time-varying magnetic fields, *IEEE Transactions on Biomedical Engineering*. 35: 577-583, 1988.
120. Bottomley, P. A. and Roemer, P. B. Homogeneous tissue model estimates of RF power deposition in human NMR studies. *In: R. L. Magin, R. P.*

- Liburdy, and B. Persson (eds.), Biological effects and safety aspects of nuclear magnetic resonance imaging and spectroscopy, 649: 144-159. New York: The New York Academy of Sciences, 1992.
121. CDRH MR Product Reporting Program and Medical Device Report Program. U.S. Department of Health and Human Services, Food and Drug Administration (FDA), 1989.
 122. Konings, M. K. and Bakker, C. J. G. Intolerable heating by resonating RF waves around guidewires. *In: International Society for Magnetic Resonance in Medicine, Seventh Scientific Meeting and Exhibition, Philadelphia, Pennsylvania, USA. 1004, 1999.*
 123. Kollias, S. S., Bernays, R., Marugg, R. A., Romanowski, B., Yonekawa, Y., and Valavanis, A. Target definition and trajectory optimization for interactive MR-guided biopsies of brain tumors in an open-configuration MRI system, *Journal of Magnetic Resonance Imaging. 8: 143-159, 1998.*
 124. Bakker, C. J., Bhagwandien, R., Moerland, M. A., and Ramos, L. M. Simulation of susceptibility artifacts in 2D and 3D Fourier transform spin-echo and gradient-echo magnetic resonance imaging, *Magnetic Resonance Imaging. 12: 767-774, 1994.*
 125. Ladd, M. E., Erhart, P., Debatin, J. F., Romanowski, B. J., Boesinger, P., and McKinnon, G. C. Biopsy needle susceptibility artifacts, *Magnetic Resonance in Medicine. 36: 646-651, 1996.*
 126. Bakker, C. J. G., Bhagwandien, R., Moerland, M. A., and Fuderer, M. Susceptibility artifacts in 2DFT spin-echo and gradient-echo imaging: the cylinder model revisited, *Magnetic Resonance Imaging. 22: 539-548, 1993.*
 127. Mueller, P. R., Stark, D. D., Simeone, J. F., Saini, S., Butch, R. J., Edelman, R. R., Wittenberg, J., and J. T. Ferrucci, J. MR-guided aspiration biopsy: needle design and clinical trials, *Radiology. 161: 605-609, 1986.*
 128. Duckwiler, G., Lufkin, R. B., Teresi, L., Spickler, E., Dion, J., Vinuela, F., Bentson, J., and Hanafee, W. Head and neck lesions: MR-guided aspiration biopsy, *Radiology. 170: 519-522, 1989.*
 129. Rubin, D. L., Rather, A. V., and Young, S. W. Magnetic susceptibility effects and their application in the development of new ferromagnetic catheters for magnetic resonance imaging, *investigative Radiology. 25: 1325-1332, 1990.*
 130. Köchli, V. D., McKinnon, G. C., Hofmann, E., and von Schulthess, G. K. Vascular interventions guided by ultrafast MR imaging: evaluation of different materials, *Magnetic Resonance in Medicine. 31: 309-314, 1994.*
 131. Leung, D. A., Debatin, J. F., Wildermuth, S., McKinnon, G. C., Holtz, D., Dumoulin, C. L., Darrow, R. D., Hofmann, E., and von Schulthess, G. K. Intravascular MR tracking catheter: preliminary experimental evaluation, *AJR. 164: 1265-1270, 1995.*
 132. Frahm, C., Gehl, H.-B., Melchert, U. H., and Weiss, H.-D. Visualization of magnetic resonance-compatible needles at 1.5 and 0.2 Tesla, *Cardiovascular and Interventional Radiology. 19: 335-340, 1996.*
 133. Lewin, J. S., Duerk, J. L., Jain, V. R., Petersilge, C. A., Chao, C. P., and Haaga, J. R. Needle localization in MR-guided biopsy and aspiration: effects of field strength, sequence design, and magnetic field orientation, *AJR. 166: 1337-1345, 1996.*

134. Kugel, H., Langen, H. J., Krahe, T., Heindel, W., and Lackner, K. Precision of MR-guided needle placement - experimental results, *MAGMA*. 4: 143-144, 1996.
135. Glowinski, A., Adam, G., Buckner, A., Neuerburg, J., van Vaals, J. J., and Gunther, R. W. Catheter visualization using locally induced, actively controlled field inhomogeneities, *Magnetic Resonance in Medicine*. 38: 253-258, 1997.
136. Adam, G., Glowinski, A., Neuerburg, J., Buckner, A., van Vaals, J. J., and Gunther, R. W. Visualization of MR-compatible catheters by electrically induced local field inhomogeneities: evaluation in vivo, *Journal of Magnetic Resonance Imaging*. 8: 209-213, 1998.
137. Hohenschuh, E. and Watson, A. D. Contrast media: theory and mechanisms of contrast-enhancing agents. *In: C. B. Higgins, H. Hricak, and C. A. Helms (eds.), Magnetic resonance imaging of the body*, 3rd edition. 1439-1464. Philadelphia: Lippincott-Raven, 1997.
138. Burl, M., Coutts, G. A., and Young, I. R. Tuned fiducial markers to identify body locations with minimal perturbation of tissue magnetization, *Magnetic Resonance in Medicine*. 36: 491-493, 1996.
139. Dumoulin, C. L., Darrow, R. D., Eisner, D. R., Tarnawski, M., Scott, K. T., and Caro, C. G. Simultaneous detection of multiple components of motion with MRI, *Journal of Computer Assisted Tomography*. 18: 652-660, 1994.
140. Zimmermann-Paul, G. G., Ladd, M. E., Pfammatter, T., Hilfiker, P. R., Quick, H. H., and Debatin, J. F. MR versus fluoroscopic guidance of a catheter/guidewire system: in vitro comparison of steerability, *Journal of Magnetic Resonance Imaging*. 8: 1177-1181, 1998.
141. Ladd, M. E., Zimmermann, G. G., McKinnon, G. C., von Schulthess, G. K., Dumoulin, C. L., Darrow, R. D., Hofmann, E., and Debatin, J. F. Visualization of vascular guidewires using MR tracking, *Journal of Magnetic Resonance Imaging*. 8: 251-253, 1998.
142. Erhart, P., Ladd, M. E., Steiner, P., Heske, N., Dumoulin, C. L., and Debatin, J. F. Tissue-independent MR tracking of invasive devices with an internal signal source, *Magnetic Resonance in Medicine*. 39: 279-284, 1998.
143. Coutts, G. A., Gilderdale, D. J., Chui, M., Kasuboski, L., and DeSouza, N. M. Integrated and interactive position tracking and imaging of interventional tools and internal devices using small fiducial receiver coils, *Magnetic Resonance in Medicine*. 40: 908-913, 1998.
144. Dumoulin, C. L., Souza, S. P., Darrow, R. D., Pelc, N. J., Adams, W. J., and Ash, S. A. Simultaneous acquisition of phase-contrast angiograms and stationary-tissue images with Hadamard encoding of flow-induced phase shifts, *Journal of Magnetic Resonance Imaging*. 1: 399-404, 1991.
145. Pelc, N. J., Bernstein, M. A., Shimakawa, A., and Glover, G. H. Encoding strategies for three-direction phase-contrast MR imaging of flow, *Journal of Magnetic Resonance Imaging*. 1: 405-413, 1991.
146. Hausmann, R., Lewin, J. S., and Laub, G. Phase-contrast MR angiography with reduced acquisition time: new concepts in sequence design, *Journal of Magnetic Resonance Imaging*. 1: 415-422, 1991.

147. Hurst, G. C., Hua, J., Duerk, J. L., and Cohen, A. M. Intravascular (catheter) NRM receiver probe: preliminary design analysis and application to canine iliofemoral imaging, *Magnetic Resonance in Medicine*. 24: 343-357, 1992.
148. Kandarpa, K., Jakab, P., Patz, S., Schoen, F. J., and Jolesz, F. A. Prototype miniature endoluminal MR imaging catheter, *Journal of Vascular & Interventional Radiology*. 4: 419-427, 1993.
149. Atalar, E., Bottomley, P. A., Ocali, O., Correia, L. C. L., Kelemen, M. D., Lima, J. A. C., and Zerhouni, E. A. High resolution intravascular MRI and MRS by using a catheter receiver coil, *Magnetic Resonance in Medicine*. 36: 596-605, 1996.
150. Ladd, M. E., Zimmermann, G. G., Quick, H. H., Debatin, J. F., Boesiger, P., von Schulthess, G. K., and McKinnon, G. C. Active MR visualization of a vascular guidewire in vivo, *Journal of Magnetic Resonance Imaging*. 8: 220-225, 1998.
151. Ocali, O. and Atalar, E. Intravascular magnetic resonance imaging using a loopless catheter antenna, *Magnetic Resonance in Medicine*. 37: 112-118, 1997.
152. Atalar, E., Kraitichman, D. L., Carkhuff, B., Lesho, J., Ocali, O., Solaiyappan, M., Guttman, M. A., and Charles, H. K., Jr. Catheter-tracking FOV MR fluoroscopy, *Magnetic Resonance in Medicine*. 40: 865-872, 1998.
153. Jolesz, F. A. Interventional and intraoperative MRI: a general overview of the field, *Journal of Magnetic Resonance Imaging*. 8: 3-7, 1998.
154. Ladd, M. E. A 0.7mm triaxial cable for significantly reducing RF heating in interventional MR. *In: International Society for Magnetic Resonance in Medicine, Seventh Scientific Meeting and Exhibition, Philadelphia, Pennsylvania, USA*. 104, 1999.

Summary of Publications

I Interventional MR imaging: Demonstration of the feasibility of the Overhauser marker enhancement (OMEN) technique

A point-like Overhauser marker was designed and evaluated in phantom experiments. The coupling scheme to the feeding line was a simple loop.

II High-accuracy MR tracking of interventional devices: The Overhauser marker enhancement (OMEN) technique

Circuit analogies were presented for the Overhauser phenomenon and a loop-gap coupled Overhauser marker. The Overhauser circuit model allowed studying dynamic responses of the NMR signal enhancement and the coupling model predicted a detuning effect when electron spin resonance occurs in the marker solution. A loop-gap marker was constructed and evaluated *in vitro*.

III A shielded Overhauser marker for MR tracking of interventional devices

A transmission line Overhauser marker was constructed. A tapered coupling section and an RF-transparent microwave shielding were designed and included in the marker's construction. The marker signal's orientation dependency was measured and explained as well as the signal's oscillating pattern. The marker's temperature distribution was simulated which revealed the center conductor's essential role as a heat sink. The marker's temperature was measured by infrared and calorimeter means, which correlated quite well with simulations. The marker's performance was verified *in vitro*.

IV A sub-voxel-sized Overhauser phantom for high-resolution studies in MRI

A sub-voxel-sized phantom was constructed where the NMR signal emitted by the phantom was enhanced by applying the Overhauser phenomenon. The use of the phantom allowed the study of the imaging system's point spread function in three dimensions.